anti-Arpc2 (EPR8533) (1:2,000; Abcam, ab133315), anti-Arhgef6/Cool2/αPIX (C23D2) (1:1,000 for immunoblot; 1:400 for immunostain; Cell Signaling, 4573), anti-Gapdh antibody (1:5,000; Millipore, MAB374), anti-GFP-horseradish peroxidase (HRP) (1:3,000; MBL, 598-7), anti–RFP-HRP (1:3,000; MBL, PM005-7), anti-FLAG M2-HRP (1:5,000; Sigma-Aldrich, A8592), anti-V5-HRP antibody (1:5,000; Life Technologies, R961-25), HRP-coupled goat anti–rabbit (1:8,000; Cappel, 55696), anti-mouse IgG (1:8,000; Cappel, 55550), Alexa Fluor 488- (1:1,000 for staining; Life Technologies, A11029), Alexa Fluor 546- (1:1,000 for staining; Life Technologies, A11003) and Alexa Fluor 568-labelled secondary antibodies (1:1,000 for staining; Life Technologies, A11011), and Alexa Fluor 647 phalloidin (1:100 for staining; Cell Signaling, 8940). Anti-FLAG M2 affinity gel (A2220) and anti-V5 agarose affinity gel (A7345) were from Sigma-Aldrich. We used three different AMPK activators: AICAR is metabolized intracellularly to ZMP (5-aminoimidazole-4-carboxamide-1-β-D-ribofuranotide), an AMP analogue. A769662 is a thienopyridone derivative that acts as an allosteric activator of the AMPK by binding to an alternative site that does not overlap with the AMP-binding site.
2-DG is a non-metabolizable glucose analogue and inhibitor of phosphohexose isomerase that inhibits glycolysis and mimics glucose starvation, increases the AMP/ATP ratio and thereby activates AMPK.

Antibodies for Pdlim5 and pS177 of Pdlim5. Six polyclonal Pdlim5 antibodies (1:1,000 for immunoblotting and immunostaining) and two polyclonal phospho-Ser177 (pS177)-Pdlim5 antibodies (1:1,000 for immunoblotting) were generated as follows. Three different peptides corresponding to mouse Pdlim5 sequences (amino acids 229–245, QGDIKQQNGPPRKHIVEC; amino acids 290–306, CTGTEHLTESENDNTKKA; and amino acids 381–397, SSGTGASVGPPQPSDQDC), as well as Ser-phosphorylated and non-phosphorylated peptides corresponding to the mouse Pdlim5 sequences surrounding Ser177 (amino acids 172–182, LHLSA(pS)GLHVS), were chemically synthesized. Rabbits were immunized five times with the keyhole limpet haemocyanin–phosphopeptide conjugates mixed with Freund's complete adjuvant and bled 7 days after the last immunization. Phosphopeptide-reactive antibody was captured by a column containing phosphopeptide-conjugated Sepharose. The antibodies were then eluted, and those reactive to sequences other than phosphoserine were removed using a column containing non-phosphorylated peptides. Specific reactivity with the targeted phosphoserine sequence was confirmed by ELISA using phosphorylated and non-phosphorylated peptides.

Cell culture and siRNA transfection. C2C12 cells (an immortalized mouse myoblast cell line) and HEK293T cells were obtained from the American Type Culture Collection. A vSMC line established from thoracic aorta of a p53-knockout mice (P53LMACO1) was purchased from Health Science Research Resources Bank. These cells were maintained in DMEM medium (Sigma-Aldrich) supplemented with 10% FCS (Equitech-Bio) and 1% penicillin–streptomycin at 37 °C in a 5% CO_2 atmosphere at constant humidity and passaged by trypsinization at 70–80% confluence. HL60 cells and RAW264.7 cells were obtained from the Japanese Collection of Research Bioresources Cell Bank and American Type Culture Collection, respectively. These cells were maintained in RPMI1640 medium with 10% FCS and 1% penicillin–streptomycin. HEK293T cells and vSMCs were transfected with plasmids using Lipofectamine 2000 reagent (Invitrogen). To knock down endogenous Pdlim5, C2C12 cells and vSMCs were transfected with siRNAs (30 nM) targeting Pdlim5 (siPdlim5-1, sense: 5′-ggaacaauaugucguggauTT-3′; antisense: 5′-auccacgacauauuguuccTT-3′; siPdlim5-2, sense: 5′-ggguaguagcuaugagaauTT-3′; antisense: 5′-auucucauagcuacuacccTT-3′) using Lipofectamine RNAiMAX (Invitrogen). To knock down endogenous Arpc2, vSMCs were transfected with siRNAs (5 nM) targeting Arpc2 (siArpc2-1, sense: 5′-ggccuauauucauacacgaTT-3′; antisense: 5′-ucguguaugaauauaggccTT-3′; siArpc2-2, sense: 5′-gaaccaggauauaauguuuTT-3′; antisense: 5′-aaacauuauauccuggguucTG-3′) using Lipofectamine RNAiMAX (Invitrogen). RAW264.7 cells (mouse leukemic monocyte macrophage cell) were used to check the effect of siRNAs against Arhgef6. RAW264.7 cells were transfected with siRNAs (50 nM) targeting Arhgef6 (siArhgef6-1, sense: 5′-gauucuuaaggugaucgaaTT-3′; antisense: 5′-uucgaucaccuuaagaaucTG-3′; siArhgef6-2, sense: 5′-gugaugaucuagaacgauuTT-3′; antisense: 5′-aaucguucuagaucaucacTG-3′) using GenMute siRNA Transfection Reagent for RAW 264.7 (SignaGen). siControl was used as a negative control. Efficiency of siRNA-mediated knockdown was confirmed at 24 and 72 h after incubation with siRNAs. AMPKα double-knockout (AMPKα1$^{-/-}$α2$^{-/-}$) MEFs (AMPKα-null MEFs)[25] were kindly provided by Dr B. Viollet (INSERM, France) and maintained in DMEM supplemented with 10% FCS, 1 mM sodium pyruvate and 1% penicillin–streptomycin at 37 °C in a 5% CO_2 atmosphere at constant humidity.

Hypoxia. Cultured cells were exposed to hypoxia for 2 h. Hypoxic conditions (1% O_2) were maintained in a MCO-5M multi-gas incubator (Sanyo).

Establishment of the KDR system. To replace endogenous Pdlim5 by EGFP-tagged recombinant Pdlim5 (WT, S177A or S177D), vSMCs were transfected with siPdlim5-2 to deplete endogenous Pdlim5. Next, 12 h after siPdlim5-2 transfection, siPdlim5-2-resistant EGFP-tagged Pdlim5 (WT, S177A or S177D) was adenovirally transduced into vSMCs, to establish the KDR system. vSMCs were incubated with adenovirus at a multiplicity of infection of 10 in DMEM supplemented with 10% FCS at 37 °C under 5% CO_2 for 30 min, with gentle mixing every 10 min, and then further incubated for 48 h before analysis.

Purification and identification of Pdlim5. C2C12 cells seeded on 15-cm dishes (2×10^6 cells per dish) were treated with 2 mM of AICAR for 1 h, harvested and lysed on ice in lysis buffer A (20 mM Tris pH 8.0, 0.5% NP-40, 0.5% CHAPS, 20% acetonitrile, 25 mM β-glycerophosphate, 10 mM NaF and protease inhibitor cocktail (Nacalai Tesque)). Lysates were incubated at 4 °C with agitation for 20 min, followed by centrifugation at 10,000 *g* for 20 min. Supernatant from six 15-cm dishes was passed through a 0.45-μm sterilization filter and loaded onto a TSK-GEL SuperQ-5PW (7.5 × 75 mm, TOSOH) anion-exchange column pre-equilibrated with column buffer A (20 mM Tris pH 8.0, 0.5% CHAPS, 20% acetonitrile, 25 mM β-glycerophosphate, 10 mM NaF). After being washed with column buffer A, proteins were eluted with a linear gradient of NaCl (0–1 M over 60 min) at a flow rate of 0.5 ml min^{-1}. Fractions (0.5 ml each) were collected and a 50-μl aliquot of each fraction was analysed by immunoblotting with anti-pACC antibody. The corresponding fractions were prepared in the presence of 0.3% TFA (trifluoroacetic acid), 0.1% OG (*n*-octyl-β-D-thioglucopyranoside) and 20% acetonitrile, and loaded onto a Protein-R (4.6 × 250 mm, Nacalai Tesque) reverse-phase HPLC column pre-equilibrated with column buffer B (0.1% TFA and 0.1% OG). After being washed with column buffer B, the proteins were eluted with a linear gradient of acetonitrile (20–80% over 60 min) at a flow rate of 0.5 ml min^{-1}. Fractions (0.5 ml each) were collected and a 25-μl aliquot of each fraction was analysed by immunoblotting with anti-pACC antibody. The corresponding fractions were again prepared in the presence of 0.3% TFA, 0.1% OG and 20% acetonitrile, and loaded onto a 5Ph-AR-300 (4.6 × 250 mm, Nacalai Tesque) reverse-phase HPLC column pre-equilibrated with column buffer B. After being washed with column buffer B, proteins were eluted with a linear gradient of acetonitrile (20–80% over 60 min) at a flow rate of 0.5 ml min^{-1}. Each fraction was analysed by SDS–PAGE and visualized by silver staining and immunoblotting with anti-pACC antibody. Target bands matching the pACC antibody cross-reacting bands were excised from the gel and analysed using matrix-assisted laser desorption/ionization-quadrupole-time-of-flight-tandem mass spectrometry (MALDI-Qq-TOF MS/MS).

Protein purification. Recombinant FLAG-tagged Pdlim5 proteins were purified as follows: HEK293T cells transfected with pEF-DEST51/cFLAG plasmid encoding WT Pdlim5, S175A Pdlim5 or S177A Pdlim5 were lysed in lysis buffer B (20 mM MOPS pH 7.5, 0.15 M NaCl, 0.5% CHAPS, 1 mM EDTA, 1 mM dithiothreitol (DTT) and protease inhibitor cocktail) and immunoprecipitated with anti-FLAG M2 agarose (Sigma-Aldrich) at 4 °C for 30 min. The beads were washed three times with wash buffer (20 mM MOPS pH 7.5, 0.3 M NaCl, 0.5% CHAPS, 1 mM EDTA, 1 mM DTT and protease inhibitor cocktail) and eluted with elution buffer (20 mM MOPS pH 7.5, 0.3 M NaCl, 0.5% CHAPS, 1 mM DTT and 0.5 mg ml^{-1} FLAG peptide (Sigma-Aldrich)) at 4 °C for 30 min. After centrifugation, the supernatants were used as recombinant FLAG-tagged proteins. Recombinant GST-Pdlim5 proteins (WT, S177A, S177D and ΔPDZ) were purified as follows: BL21 chemically competent *E. coli* (Invitrogen) were transformed with pGEX-6P-1-WT Pdlim5, pGEX-6P-1-S177A Pdlim5, pGEX-6P-1-S177D Pdlim5 or pGEX-6P-1-ΔPDZ Pdlim5, and then induced with 0.5 mM isopropyl-β-D-thiogalactoside (Sigma-Aldrich) at 25 °C for 10 h. The cells were collected by centrifugation and lysed by sonication in PBS containing 5 mM EDTA and protease inhibitor cocktail. After addition of 1% Triton X-100, the lysates were agitated at 4 °C for 30 min and pulled down with glutathione–Sepharose 4 Fast Flow (GE Healthcare) at 4 °C for 1 h. After being washed three times, the proteins were eluted with 15 mM reduced glutathione and ultrafiltered in elution buffer using a Nanosep 10K Device (Pall Life Science).

Immunoblotting. Immunoblotting was performed using the indicated antibodies. Blots were cropped such that at least one marker position is present. Uncropped full scans of the figures are supplied in Supplementary Figs 17–23.

Phosphorylation assay. Phosphorylation assays were carried out at 30 °C in a reaction volume of 10 μl containing Tris-HCl (20 mM pH 7.4), glycerol (10%), NaCl (0.3 mM), AMP (0.2 mM), MgCl2 (10 mM), γ-^{32}P ATP (GE Healthcare BioScience, 10 μCi, 1.7 pmol) and AMPK purified from rat liver (2 ng μl^{-1}). Purified mouse Pdlim5-cFLAG proteins or purified recombinant GST-fused mouse Pdlim5 proteins were used as substrates. After 60 min, reactions were terminated and ultrafiltered in PBS containing 0.1% SDS using a Nanosep 10K Device (Pall Life Science). Each fraction sample was analysed by SDS–PAGE and visualized by autoradiography. For immunoblotting with anti-pS177 antibody, recombinant GST-fused Pdlim5 proteins were incubated under the same conditions, except that ATP (0.1 mM) was included instead of γ-^{32}P ATP.

Scratch assay. KDR/EGFP-Pdlim5 (WT, S177A and S177D) cells or MEFs were plated on a collagen-coated 35-mm glass dish at a density of 5×10^5 cm^{-2}. Eight hours after plating, a scratch was made with a P-200 pipette tip and the lesions were observed for a total of 8 h. Differential interference contrast images were

recorded every 5 min using an Olympus LCV110 incubator microscope (Olympus Corporation, Tokyo, Japan). To determine cell trajectories, the centrioles of cell nuclei were tracked throughout time-lapse movies, and migration-tracking images were generated using the MetaMorph 7.1.3.0 software (MDS Analytical Technologies, Downingtown, PA, USA). Overall migration speed was calculated as the average of migration speeds measured every 5 min.

Single-cell migration assay. KDR/EGFP-Pdlim5 (WT, S177A and S177D) cells were plated on a collagen-coated 35-mm glass dish at a density of 5×10^5 cm^{-2}. Five hours after the plating, we started to observe cell migration by recording differential interference contrast images every 5 min for a total of 4 h using an Olympus LCV110 incubator microscope (Olympus Corporation).

Immunocytochemistry and fluorescence imaging. vSMCs or KDR cells were seeded on a collagen-coated 35-mm glass dishes (Asahi Techno Glass Corporation, Chiba, Japan). After cells firmly attached to the dish, they were washed once with warm PBS and fixed with 4% paraformaldehyde for 5 min at room temperature. Next, the cells were permeabilized with 0.1% Triton X-100 in PBS for 5 min at room temperature and then blocked with 1% BSA at 4 °C overnight. The next day, samples were immunostained with primary antibodies (1:1,000 in 1% BSA, 1 h). For secondary reactions, species-matched Alexa Fluor 488- or Alexa Fluor 568-labelled secondary antibody was used (1:1,000 in 1% BSA, 30 min). Just before imaging, the sample was incubated with Alexa Fluor 647-conjugated phalloidin in CGS-Sol A for 1 h. Fluorescence images of EGFP, Alexa Fluor 488, Alexa Fluor 546, Alexa Fluor 568 and Alexa Fluor 647 were recorded using an Olympus FV1000-D confocal laser scanning microscope (Olympus Corporation) equipped with a cooled charge-coupled device CoolSNAP-HQ camera (Roper Scientific, Tucson, AZ, USA) and a PLAPO ×60 oil-immersion objective lens. To measure the paxillin-positive area, all intensity profiles were analysed using the MetaMorph 7.1.3.0 software.

Time-lapse imaging of KDR/EGFP-Pdlim5 cells. KDR/EGFP-Pdlim5 (WT and S177A) cells were seeded on collagen-coated 35-mm glass dishes at a density of 4×10^4 cm^{-2}. Five hours after plating, cells were treated with AICAR (2 mM). The fluorescence images were recorded from 10 min before to 60 min after AICAR treatment, using an Olympus IX-81 inverted fluorescence microscope (Olympus Corporation) equipped with a cooled charge-coupled device CoolSNAP-HQ camera (Roper Scientific) and a PLAPO ×60 oil-immersion objective lens controlled by MetaMorph version 7.1.3.0. An EGFP image was obtained every 30 s through a U-MNIBA2 filter (Olympus Corporation), which had a 470–495 excitation filter and a 510–550 emission filter. Cells were maintained on a microscope at 37 °C with a 5% carbon dioxide mixture using a stage-top incubator (Tokai Hit). MetaMorph was used to convert a series of time-lapse images to video format.

Measurement of the GTP-bound form of Rac1, RhoA and Cdc42. KDR cells at 50%confluence were incubated for 24 h in FCS-free DMEM to starve the cells, and then treated with 10% FCS for 30 min. Cell lysates were collected and levels of activated GTP-bound Rac1, RhoA and Cdc42 were determined using the G-LISA Rac1 Activation Assay Biochem Kit (BK126, Cytoskeleton Inc., CO, USA), G-LISA RhoA Activation Assay Biochem Kit (BK121, Cytoskeleton Inc.) and G-LISA Cdc42 Activation Assay Biochem Kit (BK127, Cytoskeleton Inc.), respectively.

Imaging of Rho GTPases (Rac1, RhoA and Cdc42) activities. To visualize activities of Rho GTPases in living cells, we established a vSMC cell line stably expressing a Rho GTPase FRET biosensor consisting of cyan fluorescent protein (CFP) and yellow fluorescent protein (YFP), as previously described[43]. In brief, vSMCs were transfected with the CFP/YFP-type FRET biosensor gene for Rho GTPases, using the PiggyBac retrotransposon-mediated gene transfer system, and then cultured for 2 w with 10 μg ml^{-1} blasticidin S to select for vSMCs stably expressing the FRET biosensor (Raichu-Rac1, RhoA or Cdc42/vSMC). Next, a KDR system for vSMCs expressing Raichu-Rac1, Raichu-RhoA or Rhaicu-Cdc42 was established as described above, except for the use of an adenovirus encoding non-tagged Pdlim5 (WT, S177A and S177D)-T2A-mCherry instead of EGFP-tagged Pdlim5 (Raichu-Rac1, RhoA or Cdc42/KDR-Pdlim5-T2A-mCherry). Forty-eight hours after the transduction of Pdlim5-T2A-mCherry, Raichu-Rac1, RhoA or Cdc42/KDR-Pdlim5-T2A-mCherry cells were re-plated on collagen-coated glass-base dishes. All experiments were performed at 37 °C in a 5% CO_2 atmosphere using a heating chamber. Dual images for CFP and YFP were obtained on a laser scanning microscope (LSM710, Zeiss) using an excitation wavelength of 405 nm and emission bandpass filters of 458–510 nm for CFP and 517–598 nm for YFP. After background subtraction, FRET/CFP ratio images were created using the LSM software ZEN2011 (Zeiss) and displayed as an intensity-modulated display image. For quantitative FRET analysis, the FRET/CFP ratio of each cell was calculated by dividing the fluorescence intensity of YFP by that of CFP over the total cellular area.

GST pull-down assay. For identification of proteins associated with Pdlim5, 20 μg of purified GST-tagged Pdlim5 WT or S177D-Pdlim5 was immobilized on glutathione–Sepharose beads and incubated at 4 °C for 2 h with cell lysate from 2×10^9 U937 cells in lysis buffer (30 mM MOPS pH 7.5, 150 mM NaCl, 0.5% Triton-X100, 1.5 mM $MgCl_2$, 1 mM EGTA, 1 mM DTT and protease inhibitor cocktail). After three washes of the beads with lysis buffer, associated proteins were eluted in elution buffer (30 mM MOPS pH 7.5, 500 mM NaCl, 0.5% Triton-X100, 1.5 mM $MgCl_2$, 1 mM EGTA, 1 mM DTT and protease inhibitor cocktail) and then subjected to silver staining and high-sensitivity shotgun liquid chromatography–mass spectrometry (LTQ Orbitrap ELITE, Thermo Scientific).

F-actin binding assay of AMPK. F-actin binding assays were performed using the Actin Binding Protein Biochem Kit (BK001, Cytoskeleton, Inc.) according to the manufacturer's protocol, with minor modifications. Briefly, 1 μl of F-actin (21 μM actin) in actin polymerization buffer (100 mM KCl, 2 mM $MgCl_2$, 0.5 mM ATP, 0.2 mM Tris-HCl, pH 8.0) was mixed with 0.5 μl of purified AMPK (200 ng μl^{-1}) in the presence or absence of GST-tagged WT-Pdlim5 and 1 μl of α-actinin (1 μg μl^{-1}) in 60 μl reaction volume, incubated for 1 h at 24 °C and then centrifuged at 150,000 *g* for 1.5 h at 24 °C, to pellet the F-actin polymer and associated proteins. Equal amounts of pellet (P) and supernatant (S) were resolved by SDS–PAGE and analysed by immunoblotting with the indicated antibodies.

Statistical analyses. Box plots show the entire population. Other data are expressed as means ± s.e.m. Two-tailed Student's *t*-test was used to analyse differences between two groups. Differences among multiple groups were compared by one-way analysis of variance, followed by a *post-hoc* comparison with Dunnett's method using the JMP 8.0.1 software (SAS Institute Inc., Cary, NC, USA). $P < 0.01$ was considered to indicate statistically significant differences.

References

1. Carling, D., Mayer, F. V., Sanders, M. J. & Gamblin, S. J. AMP-activated protein kinase: nature's energy sensor. *Nat. Chem. Biol.* **7,** 512–518 (2011).
2. Lee, J. H. *et al.* Energy-dependent regulation of cell structure by AMP-activated protein kinase. *Nature* **447,** 1017–1020 (2007).
3. Zhang, L., Li, J., Young, L. H. & Caplan, M. J. AMP-activated protein kinase regulates the assembly of epithelial tight junctions. *Proc. Natl Acad. Sci. USA* **103,** 17272–17277 (2006).
4. Nakano, A. *et al.* AMPK controls the speed of microtubule polymerization and directional cell migration through CLIP-170 phosphorylation. *Nat. Cell Biol.* **12,** 583–590 (2010).
5. Bae, H. B. *et al.* AMP-activated protein kinase enhances the phagocytic ability of macrophages and neutrophils. *FASEB J.* **25,** 4358–4368 (2011).
6. Kondratowicz, A. S., Hunt, C. L., Davey, R. A., Cherry, S. & Maury, W. J. AMP-activated protein kinase is required for the macropinocytic internalization of ebolavirus. *J. Virol.* **87,** 746–755 (2013).
7. Parsons, J. T., Horwitz, A. R. & Schwartz, M. A. Cell adhesion: integrating cytoskeletal dynamics and cellular tension. *Nat. Rev. Mol. Cell Biol.* **11,** 633–643 (2010).
8. Wu, Y. I. *et al.* A genetically encoded photoactivatable Rac controls the motility of living cells. *Nature* **461,** 104–108 (2009).
9. Sanz-Moreno, V. *et al.* Rac activation and inactivation control plasticity of tumor cell movement. *Cell* **135,** 510–523 (2008).
10. Campellone, K. G. & Welch, M. D. A nucleator arms race: cellular control of actin assembly. *Nat. Rev. Mol. Cell Biol.* **11,** 237–251 (2010).
11. Ridley, A. J. Life at the leading edge. *Cell* **145,** 1012–1022 (2011).
12. Dihu, J. B., Abudayyeh, I., Saudye, H. A. & Gurujal, R. Cilostazol: a potential therapeutic option to prevent in-stent restenosis. *J. Am. Coll. Cardiol.* **57,** 2035–2036 (2011).
13. Nissen, S. E. *et al.* Comparison of pioglitazone vs glimepiride on progression of coronary atherosclerosis in patients with type 2 diabetes: the PERISCOPE randomized controlled trial. *JAMA* **299,** 1561–1573 (2008).
14. Bailey, C. J. Metformin: effects on micro and macrovascular complications in type 2 diabetes. *Cardiovasc. Drugs Ther.* **22,** 215–224 (2008).
15. Esfahanian, N. *et al.* Effect of metformin on the proliferation, migration, and MMP-2 and -9 expression of human umbilical vein endothelial cells. *Mol. Med. Rep.* **5,** 1068–1074 (2012).
16. Ridley, A. J. *et al.* Cell migration: integrating signals from front to back. *Science* **302,** 1704–1709 (2003).
17. Gruzman, A., Babai, G. & Sasson, S. Adenosine monophosphate-activated protein kinase (AMPK) as a new target for antidiabetic drugs: a review on metabolic, pharmacological and chemical considerations. *Rev. Diabetic Studies* **6,** 13–36 (2009).
18. te Velthuis, A. J. & Bagowski, C. P. PDZ and LIM domain-encoding genes: molecular interactions and their role in development. *Sci. World J.* **7,** 1470–1492 (2007).
19. Zheng, Q. & Zhao, Y. The diverse biofunctions of LIM domain proteins: determined by subcellular localization and protein-protein interaction. *Biol. Cell* **99,** 489–502 (2007).

20. Lasorella, A. & Iavarone, A. The protein ENH is a cytoplasmic sequestration factor for Id2 in normal and tumor cells from the nervous system. *Proc. Natl Acad. Sci. USA* **103,** 4976–4981 (2006).
21. Yoshizaki, H. *et al.* Activity of Rho-family GTPases during cell division as visualized with FRET-based probes. *J. Cell Biol.* **162,** 223–232 (2003).
22. Feng, Q., Baird, D. & Cerione, R. A. Novel regulatory mechanisms for the Dbl family guanine nucleotide exchange factor Cool-2/alpha-Pix. *EMBO J.* **23,** 3492–3504 (2004).
23. Matsuda, C. *et al.* Affixin activates Rac1 via betaPIX in C2C12 myoblast. *FEBS Lett.* **582,** 1189–1196 (2008).
24. Viollet, B. *et al.* AMPK: Lessons from transgenic and knockout animals. *Front. Biosci. (Landmark Ed)* **14,** 19–44 (2009).
25. Laderoute, K. R. *et al.* 5′-AMP-activated protein kinase (AMPK) is induced by low-oxygen and glucose deprivation conditions found in solid-tumor microenvironments. *Mol. Cell Biol.* **26,** 5336–5347 (2006).
26. Faubert, B. *et al.* AMPK is a negative regulator of the Warburg effect and suppresses tumor growth in vivo. *Cell Metab.* **17,** 113–124 (2013).
27. Cheng, H. *et al.* Loss of enigma homolog protein results in dilated cardiomyopathy. *Circ. Res.* **107,** 348–356 (2010).
28. Horiuchi, Y. *et al.* Experimental evidence for the involvement of PDLIM5 in mood disorders in hetero knockout mice. *PLoS ONE* **8,** e59320 (2013).
29. Rosenberger, G., Jantke, I., Gal, A. & Kutsche, K. Interaction of alphaPIX (ARHGEF6) with beta-parvin (PARVB) suggests an involvement of alphaPIX in integrin-mediated signaling. *Hum. Mol. Genet.* **12,** 155–167 (2003).
30. Mishima, W. *et al.* The first CH domain of affixin activates Cdc42 and Rac1 through alphaPIX, a Cdc42/Rac1-specific guanine nucleotide exchanging factor. *Genes Cells* **9,** 193–204 (2004).
31. Cabodi, S., del Pilar Camacho-Leal, M., Di Stefano, P. & Defilippi, P. Integrin signalling adaptors: not only figurants in the cancer story. *Nat. Rev. Cancer* **10,** 858–870 (2010).
32. Wickstrom, S. A., Lange, A., Montanez, E. & Fassler, R. The ILK/PINCH/parvin complex: the kinase is dead, long live the pseudokinase! *EMBO J.* **29,** 281–291 (2010).
33. Yamaji, S. *et al.* Affixin interacts with alpha-actinin and mediates integrin signaling for reorganization of F-actin induced by initial cell-substrate interaction. *J. Cell Biol.* **165,** 539–551 (2004).
34. Nakagawa, N. *et al.* ENH, containing PDZ and LIM domains, heart/skeletal muscle-specific protein, associates with cytoskeletal proteins through the PDZ domain. *Biochem. Biophys. Res. Commun.* **272,** 505–512 (2000).
35. Michaelson, D. *et al.* Differential localization of Rho GTPases in live cells: regulation by hypervariable regions and RhoGDI binding. *J. Cell Biol.* **152,** 111–126 (2001).
36. Johnston, S. A., Bramble, J. P., Yeung, C. L., Mendes, P. M. & Machesky, L. M. Arp2/3 complex activity in filopodia of spreading cells. *BMC Cell Biol.* **9,** 65 (2008).
37. Suraneni, P. *et al.* The Arp2/3 complex is required for lamellipodia extension and directional fibroblast cell migration. *J. Cell Biol.* **197,** 239–251 (2012).
38. Wu, C. *et al.* Arp2/3 is critical for lamellipodia and response to extracellular matrix cues but is dispensable for chemotaxis. *Cell* **148,** 973–987 (2012).
39. Hotulainen, P. & Lappalainen, P. Stress fibers are generated by two distinct actin assembly mechanisms in motile cells. *J. Cell Biol.* **173,** 383–394 (2006).
40. Sander, E. E., ten Klooster, J. P., van Delft, S., van der Kammen, R. A. & Collard, J. G. Rac downregulates Rho activity: reciprocal balance between both GTPases determines cellular morphology and migratory behavior. *J. Cell Biol.* **147,** 1009–1022 (1999).
41. Chauhan, B. K., Lou, M., Zheng, Y. & Lang, R. A. Balanced Rac1 and RhoA activities regulate cell shape and drive invagination morphogenesis in epithelia. *Proc. Natl Acad. Sci. USA* **108,** 18289–18294 (2011).
42. Kovar, D. R., Harris, E. S., Mahaffy, R., Higgs, H. N. & Pollard, T. D. Control of the assembly of ATP- and ADP-actin by formins and profilin. *Cell* **124,** 423–435 (2006).
43. Aoki, K., Komatsu, N., Hirata, E., Kamioka, Y. & Matsuda, M. Stable expression of FRET biosensors: a new light in cancer research. *Cancer Sci.* **103,** 614–619 (2012).

Acknowledgements

This research was supported by the Japan Society for the Promotion of Science (JSPS) through the Funding Program for Next-Generation World-Leading Researchers (NEXT Program), which was initiated by the Council for Science and Technology Policy (CSTP); grants-in-aid from the Ministry of Health, Labour and Welfare of Japan; grants-in-aid from the Ministry of Education, Culture, Sports, Science and Technology of Japan; and grants-in-aid from the Japan Society for the Promotion of Science. This research was also supported by grants from the Japan Heart Foundation, the Japan Cardiovascular Research Foundation, the Japan Medical Association, the Japan Intractable Diseases Research Foundation, the Uehara Memorial Foundation, the Takeda Science Foundation, the Ichiro Kanehara Foundation, the Inoue Foundation for Science, the Mochida Memorial Foundation, a Heart Foundation/Novartis Grant for Research Award on Molecular and Cellular Cardiology, the Japan Foundation of Applied Enzymology, the Naito Foundation, the Banyu Foundation and Showa Houkoukai. We thank Hitoshi Miyagi, Kenichi Kondo (Olympus Corporation) and Masako Yamaguchi (Carl Zeiss Microscopy Corporation) for technical advice regarding microscopy; Saori Ikezawa, Eri Takata and Keiko Singu for technical assistance; and Yuko Okada for secretarial support.

Authors contributions

Y.Y. and O.T. designed and conducted the study, performed most of the experiments and wrote the manuscript. S.T. designed and wrote the manuscript. A.N. discussed the results and helped to write the manuscript. H.K. and K.T. performed the proteomic analysis. H.K. conducted and supported the biological experiments. N.I. performed the biochemical experiments and helped to generate plasmids. S.H., S.Y., Y.S., K.M. and Y.A. discussed the results and reviewed the manuscript. Y.L. H.A., M.A. and T.M. discussed the results. M.K. supervised all work.

Additional information

Supplementary Information accompanies this paper at http://www.nature.com/naturecommunications

Competing financial interests: The authors declare no competing financial interests.

Reprints and permission information is available online at http://npg.nature.com/reprintsandpermissions/

How to cite this article: Yan, Y. *et al.* Augmented AMPK activity inhibits cell migration by phosphorylating the novel substrate Pdlim5. *Nat. Commun.* 6:6137 doi: 10.1038/ncomms7137 (2015).

Biomaterials 35 (2014) 7839–7850

Contents lists available at ScienceDirect

Biomaterials

journal homepage: www.elsevier.com/locate/biomaterials

Excitation propagation in three-dimensional engineered hearts using decellularized extracellular matrix

Haruyo Yasui [a], Jong-Kook Lee [b, *], Akira Yoshida [a], Teruki Yokoyama [a], Hiroyuki Nakanishi [a], Keiko Miwa [b], Atsuhiko T. Naito [d], Toru Oka [a], Hiroshi Akazawa [d], Junichi Nakai [e], Shigeru Miyagawa [c], Yoshiki Sawa [c], Yasushi Sakata [a], Issei Komuro [d, *]

[a] Department of Cardiovascular Medicine, Osaka University Graduate School of Medicine, Japan
[b] Department of Cardiovascular Regenerative Medicine, Osaka University Graduate School of Medicine, 2-2 Yamada-oka, Suita 565-0871, Japan
[c] Department of Cardiovascular Surgery, Osaka University Graduate School of Medicine, Japan
[d] Department of Cardiovascular Medicine, The University of Tokyo Graduate School of Medicine, 7-3-1 Hongo, Bunkyo-ku, Tokyo 113-8655, Japan
[e] Saitama University Brain Science Institute, Japan

ARTICLE INFO

Article history:
Received 16 May 2014
Accepted 28 May 2014
Available online 20 June 2014

Keywords:
Cardiac tissue engineering
Organ culture
ECM (extracellular matrix)
Scaffold
Electrophysiology

ABSTRACT

Engineering of three-dimensional (3D) cardiac tissues using decellularized extracellular matrix could be a new technique to create an "organ-like" structure of the heart. To engineer artificial hearts functionally comparable to native hearts, however, much remain to be solved including stable excitation-propagation. To elucidate the points, we examined conduction properties of engineered tissues. We repopulated the decellularized hearts with neonatal rat cardiac cells and then, we observed excitation-propagation of spontaneous beatings using high resolution cameras. We also conducted immunofluorescence staining to examine morphological aspects. Live tissue imaging revealed that GFP-labeled-isolated cardiac cells were migrated into interstitial spaces through extravasation from coronary arteries. Engineered hearts repopulated with Ca^{2+}-indicating protein (GCaMP2)-expressing cardiac cells were subjected to optical imaging experiments. Although the engineered hearts generally showed well-organized stable excitation-propagation, the hearts also demonstrated arrhythmogenic propensity such as disorganized propagation. Immunofluorescence study revealed randomly-mixed alignment of cardiomyocytes, endothelial cells and smooth muscle cells. The recellularized hearts also showed disarray of cardiomyocytes and markedly decreased expression of connexin43. In conclusion, we successfully demonstrated that the recellularized hearts showed dynamic excitation-propagation as a "whole organ". Our strategy could provide prerequisite information to construct a 3D-engineered heart, functionally comparable to the native heart.

1. Introduction

Heart diseases are one of the leading causes of mortality worldwide [1]. Despite of recent progress in heart failure treatment, heart transplantation is still considered the final destination therapy for patients with end-stage heart failure refractory to conventional therapies. However, the benefits of heart transplantation are limited due to the shortage of donor hearts. In this context, myocardial regeneration therapy has emerged as a new therapeutic approach to treat severe heart failure. Although several clinical trials have been conducted [2], most therapies involved repairing specific regions of the heart and not the entire heart. Large-scale replacement of cardiac cells is a prerequisite for effective treatment of end-stage heart failure.

For this purpose, a new technique for engineering three-dimensional (3D) organ-like tissue using decellularized extracellular matrix (ECM) was reported for the heart [3], lung [4,5], kidney [6,7], and liver [8]. This technique has already been applied clinically for the engineering of airway [9] or heart valves [10]. A recent paper showed that induced pluripotent stem cell-derived cardiovascular progenitor cells repopulated in a decellularized heart and successfully proliferated, then differentiated into cardiovascular cells [11]. This paper also demonstrated that repopulated induced pluripotent stem cell-derived cells exhibited contraction and electrical activity, but reconstructed heart function was evaluated in the small regions of the heart. To date, only limited information is available regarding the function of a totally engineered organ.

* Corresponding authors.
E-mail address: jlee@cardiology.med.osaka-u.ac.jp (J.-K. Lee).

http://dx.doi.org/10.1016/j.biomaterials.2014.05.080
0142-9612/

Evaluation of arrhythmogenicity as a whole organ will be indispensable to construct a functionally comparable 3D engineered heart. In the present study, we hypothesized that recellularized hearts show well-organized conduction as native hearts. To elucidate the point, we investigated excitation–propagation properties of the recellularized heart by live imaging system using Ca^{2+}-indicating protein (GCaMP2) [31].

2. Materials and methods

2.1. Animals

The study was carried out under the supervision of the Animal Research Committee of Osaka University and in accordance with the Japanese Act on Welfare and Management of Animals. The experimental protocol was approved by the Animal Care and Use Committee of the Osaka University Graduate School of Medicine.

2.2. Perfusion and decellularization of rat hearts

Adult female Wistar rats (10–12-weeks-old) were anesthetized and systemic heparinization was followed by a median sternotomy. After ligating the caval veins, the heart was removed from the chest. A 2-mm cannula was inserted into the ascending aorta to enable Langendorff antegrade coronary perfusion. The right atrium was opened and an incision was made to create an atrial septal defect followed by the ligation of pulmonary artery and veins. Heparinized PBS containing 10 μM ATP was perfused for 15–30 min, followed by perfusion with 0.5% sodium dodecyl sulfate (SDS) in deionized water overnight. After washing with deionized water for 15 min, the heart was perfused with 1% Triton-X100 in deionized water for 30 min, followed by washing with antibiotic-containing PBS (100 U/ml penicillin (Invitrogen, Carlsbad, CA, USA), 100 μg/mL streptomycin (Invitrogen) and 1.25 μg/mL amphotericin B (Sigma–Aldrich, St. Louis, MO, USA)).

2.3. Isolation and preparation of rat neonatal cardiac cells

One-day-old neonatal pups were sacrificed. Their hearts were removed and placed immediately into a Petri dish containing Hank's Balanced Salt Solution (HBSS) on ice. After removing the connective tissue, the hearts were minced with scissors or blades. Trypsin (Neonatal Cardiomyocyte Isolation System, Worthington Biochemical Corporation, Lakewood, NJ, USA) was added to the dish to a final concentration of 50 μg/mL, and incubated overnight at 4 °C. Then, trypsin inhibitor reconstituted with HBSS and collagenase reconstituted with L-15 medium were added to the dish. The tissue was placed in a 37 °C shaker bath for about 35 min. The tissue was then strained through a 100-μm cell strainer and washed with L-15 medium 3 times. After centrifuging the tissue, the pellet was collected and resuspended in 30 mL of M199 (Invitrogen) with 10% FBS (BioWest, Kansas City, MO, USA), 100 U/mL penicillin (Invitrogen), 100 μg/mL streptomycin (Invitrogen), and EGM-2 Single Quots (CC-4176, Lonza, Allendale, NJ, USA) except FBS and GA-1000.

2.4. Recellularization of decellularized hearts

Approximately 1.0×10^8 cells were suspended in M199 (Invitrogen) with 10% FBS (BioWest), 100 U/mL penicillin (Invitrogen), 100 μg/mL streptomycin

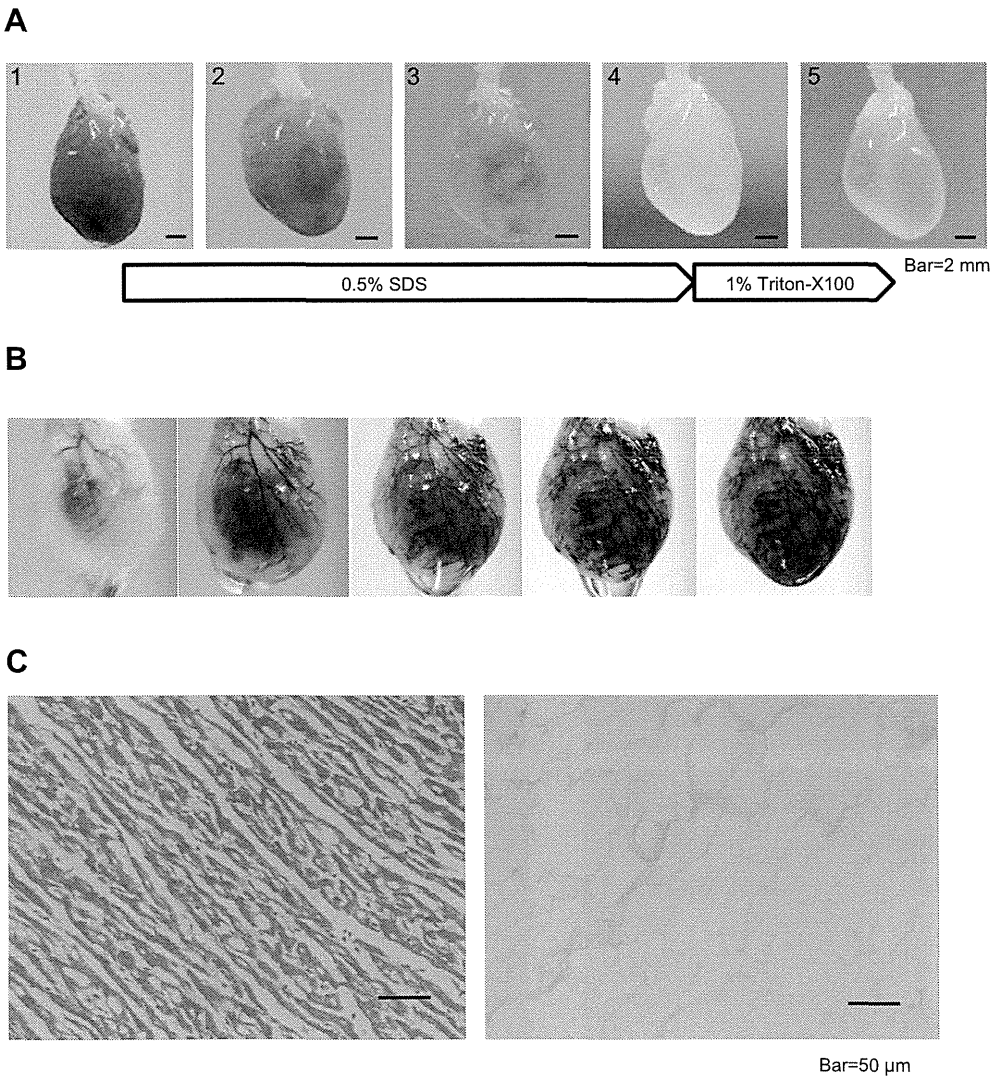

Fig. 1. Decellularization of rat hearts. (A) Macroscopic images of rat hearts during decellularization procedure: before decellularization (1); during 0.5% SDS solution perfusion (2–3); after overnight 0.5% SDS solution perfusion (4); after 1% TritonX-100 solution perfusion (5). Bars indicate 2 mm. (B) Visualization of the architecture of perfused coronary artery of decellularized extracellular matrix. (Evans blue solution was infused through aorta). (C) Microscopic structures of cadaveric (left) and decellularized (right) rat hearts (H–E staining). No nuclear staining was observed in decellularized extracellular matrix. Bars indicate 50 μm.

(Invitrogen), and EGM-2 Single Quots (CC-4176, Lonza) except FBS and GA-1000. Seeded cells consisting of cardiomyocytes, fibroblasts, and endothelial cells were infused through a T-shaped stopcock placed in the line. Recellularized rat hearts were perfused continuously and maintained in 5% CO_2 atmosphere. The culture medium was first changed at day 2 or day 3 with M199 (Invitrogen) containing 10% FBS (BioWest), 100 U/mL penicillin (Invitrogen), 100 μg/mL streptomycin (Invitrogen), and 10 μM cytosine arabinoside (Sigma–Aldrich), but without growth factors and then every 48–72 h.

2.5. Histology and immunofluorescence

We fixed rat cadaveric hearts, decellularized hearts, and recellularized hearts with 4% paraformaldehyde and cryosectioned them. This was followed by hematoxylin–eosin staining and immunostaining. We permeabilized the slides with 0.25% TritonX-100 for 20 min and blocked slides with PBS containing 10% BSA and 0.1% TritonX-100 for 60 min at RT. The samples were incubated overnight at 4 °C with the following primary antibodies: anti-sarcomeric alpha actinin antibody (mouse monoclonal 1:500; Abcam, Cambridge, UK), anti-sarcomeric alpha actinin

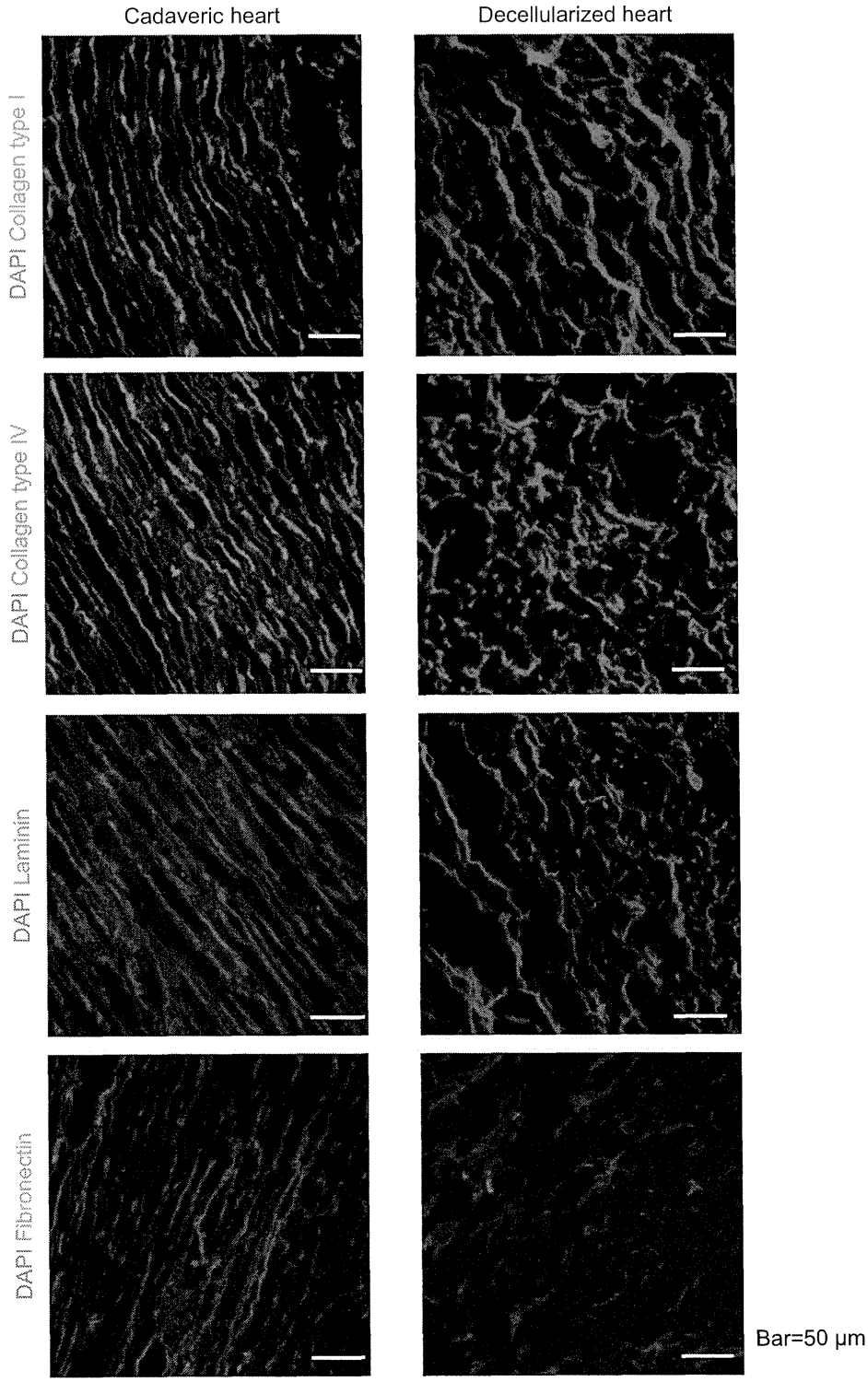

Fig. 2. Immunofluorescent staining of ECM in cadaveric and decellularized rat hearts. Collagen type I, collagen type IV, laminin, and fibronectin were maintained in decellularized (right) rat hearts as in cadaveric (left) hearts, but no nuclei was stained in decellularized (right) rat hearts. Bars indicate 50 μm.

antibody (rabbit polyclonal 1:100; Abcam), anti-laminin antibody (rabbit polyclonal 1:200; Abcam), anti-fibronectin antitibody (rabbit polyclonal 1:200; Abcam), anti-collagen IV antibody (rabbit polyclonal 1:200; Abcam), anti-collagen I antibody (rabbit polyclonal 1:200; Abcam), anti-connexin43 (Cx43) antibody (rabbit polyclonal 1:200; Invitrogen), anti-CD31 antibody (mouse monoclonal 1:100; Abcam), and anti-actin, alpha-smooth muscle-Cy3™ antibody (mouse monoclonal 1:500; Sigma–Aldrich). The samples were then incubated for 1 h with a 1:200 dilution of appropriate secondary antibodies. We embedded the samples in mounting medium containing DAPI (ProLong® Gold Antifade Reagent with DAPI; Invitrogen). Immunofluorescence images were acquired using a microscope (FSX: Olympus, Tokyo, Japan; Biorevo: Keyence, Osaka, Japan).

2.6. Western blot analysis

The frozen samples of an adult rat heart and engineered hearts were homogenized, and proteins were extracted on ice in a buffer solution containing 0.15 M NaCl, 1% NP-40, 50 mM Tris–HCl (pH 8.0), 0.5% sodium deoxycholate, 0.1% SDS and a cocktail of protease inhibitor (Complete, Mini, EDTA-free, Roche, Basel, Switzerland) and phosphatase inhibitor (PhosStop, 20 Tablets, Roche, Basel, Switzerland). Total protein (10 μg/lane) was electrophoresed and separated on an Extra PAGE One Precast Gel (nacalai tesque, Kyoto, Japan). After separation, proteins were transferred onto nitrocellulose membrane sheets (GE Healthcare Japan, Tokyo, Japan). Following transfer, the membrane was blocked in 5% low-fat dry milk in TBS-T at RT for 1 h. Then, the membrane was incubated at 4 °C overnight with following primary antibodies: sarcomeric alpha actinin (mouse monoclonal 1:500; Abcam), myosin heavy chain (MYH) (rabbit polyclonal 1:500; Santa Cruz, Dallas, TX, USA), cardiac troponin I (rabbit polyclonal 1:1000; Abcam), Cx43 (mouse monoclonal 1:1000; Invitrogen), VE-cadherin (goat polyclonal 1:500; Santa Cruz) or GAPDH (rabbit monoclonal 1:5000; Cell Signaling Technology, Danvers, MA, USA). Immunoreactive bands were visualized using an enhanced chemiluminescence (ECL) detection system (Pierce Western Blotting Substrate Plus, Thermo Fisher Scientific, Waltham, MA, USA) and an image analyzer (ImageQuant LAS 4000mini, GE Healthcare Japan).

2.7. Transmission electron microcopy

Decellularized and recellularized hearts were fixed using 2.5% glutaraldehyde (Wako, Osaka, Japan) in 0.1 M phosphate buffer (pH 7.4) through coronary perfusion; they were sectioned into 1-mm pieces and placed in 2.5% glutaraldehyde solution for 2 h. The samples were post-fixed with 1% osmium tetroxide and dehydrated with ethanol. They were embedded in epoxy resin and sectioned into 80 nm slices by

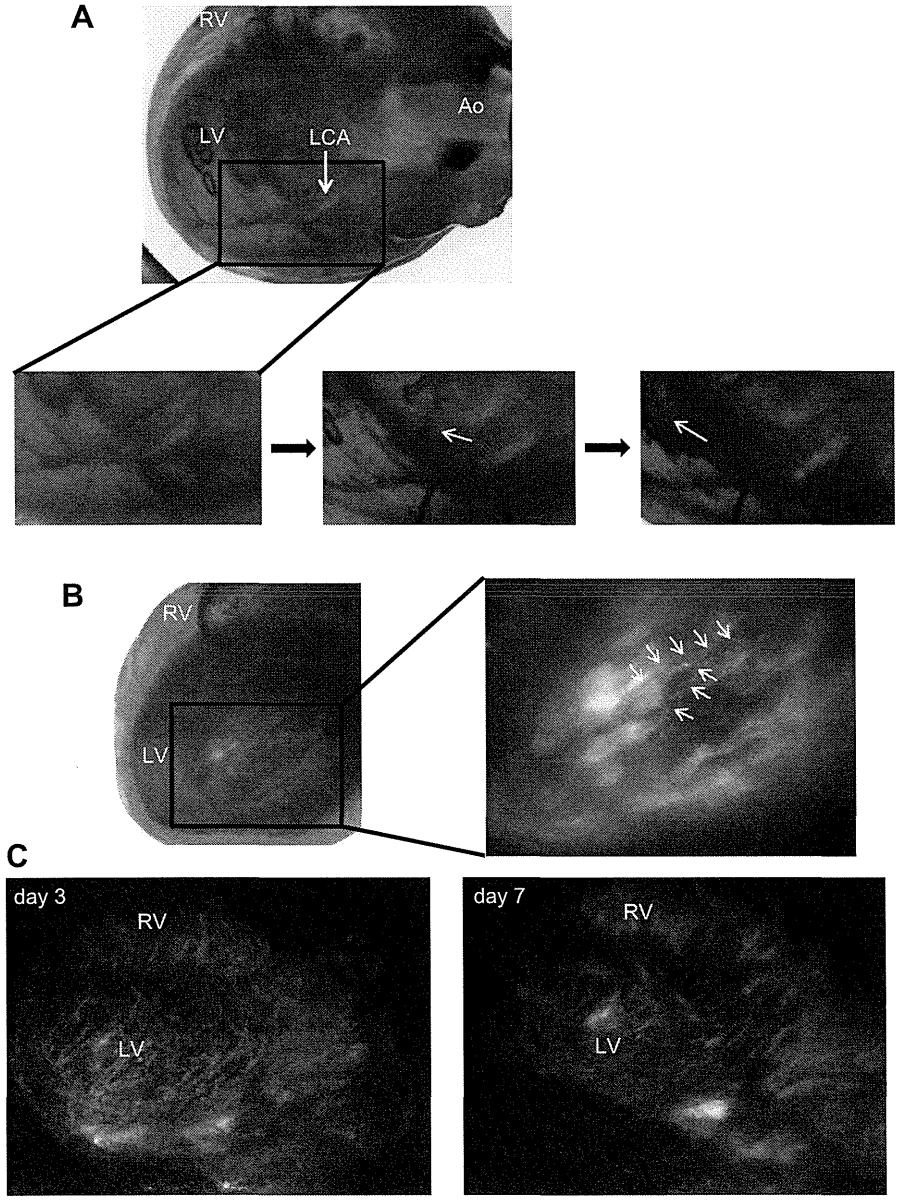

Fig. 3. Extravasation of GFP-labeled neonatal rat cardiac cells. (A) Dispersion of GFP-labeled isolated cardiac cells. GFP-labeled cells were antegradely infused into the coronary artery through aorta (upper panel). Time course of the migration of the cells is shown in magnified images (lower panels): After injection: 4 min (left), 11 min (middle), 16 min (right). The GFP-labeled cells (arrows) migrated into the interstitial spaces through extravasation. (B) At day 2, substantial portion of the seeded cells was observed in the interstitial spaces. Arrows show decellularized vessel structure. The seeded cells existed in the interstitial matrix as well as in the lumens of coronary arteries. (C) GFP-positive cells were retained in the heart for 7 days. Day 3 (left) and day 7 (right). GFP-positive cells were observed throughout the heart but inhomogeneously.

ultramicrotome. Ultra-thin sections were prepared and examined under an electron microscope (H-7650, Hitachi, Tokyo, Japan).

2.8. Transfection of adenovirus encoding GFP and GCaMP2

Isolated neonatal rat cardiac cells were infected with adenovirus encoding GFP and GCaMP2 [31] at a multiplicity of infection (m.o.i.) of 10 and 20, respectively. GFP and GCaMP2 expressing cardiac cells were suspended with the culture medium and injected into the decellularized hearts as described above.

2.9. Electrical and mechanical experiments

Electrocardiograms (ECGs) were recorded in epicardial surface of ventricle. Signals were then digitized through an AD converter (Digidata 1320, Molecular Devices, Sunnyvale, CA, USA) and analyzed with softwares (Axoscope, Molecular Devices; OriginPro, OriginLab Corporation, Northampton, MA, USA). Intraventricular pressures were recorded through a catheter (1.4Fr-Mikro-Tip™ Catheter Transducer, Millar, Bella Vista, NSW, Australia) with an amplifier (PowerLab, AD Instruments Inc., Dunedin, New Zealand).

2.10. Live tissue imaging

We observed recellularized hearts temporarily under a fluorescent stereomicroscope (Leica Microsystems Ltd., Wetzlar, Germany). Recellularized hearts were placed in culture flasks and their fluorescent images were recorded with a GFP-band path filter. Data analysis was performed using custom MALTAB software (MathWorks, Natick, MA, USA). Before fixation, calcium transient (CaT) of the recellularized hearts were optically recorded using a high-resolution CMOS camera (MiCAM02, Brainvision, Tokyo, Japan). Data analysis was performed using custom-made software (BV_Ana, Brainvision). Fast Fourier Transform (FFT) analyses were conducted using software (OriginPro, OriginLab Corporation).

3. Results

3.1. Decellularization of adult rat hearts

Perfusion of 0.5% SDS and subsequent application of 1% Triton-X100 removed all the cellular components from the hearts, leaving behind the extracellular matrices (Fig. 1A). Histological

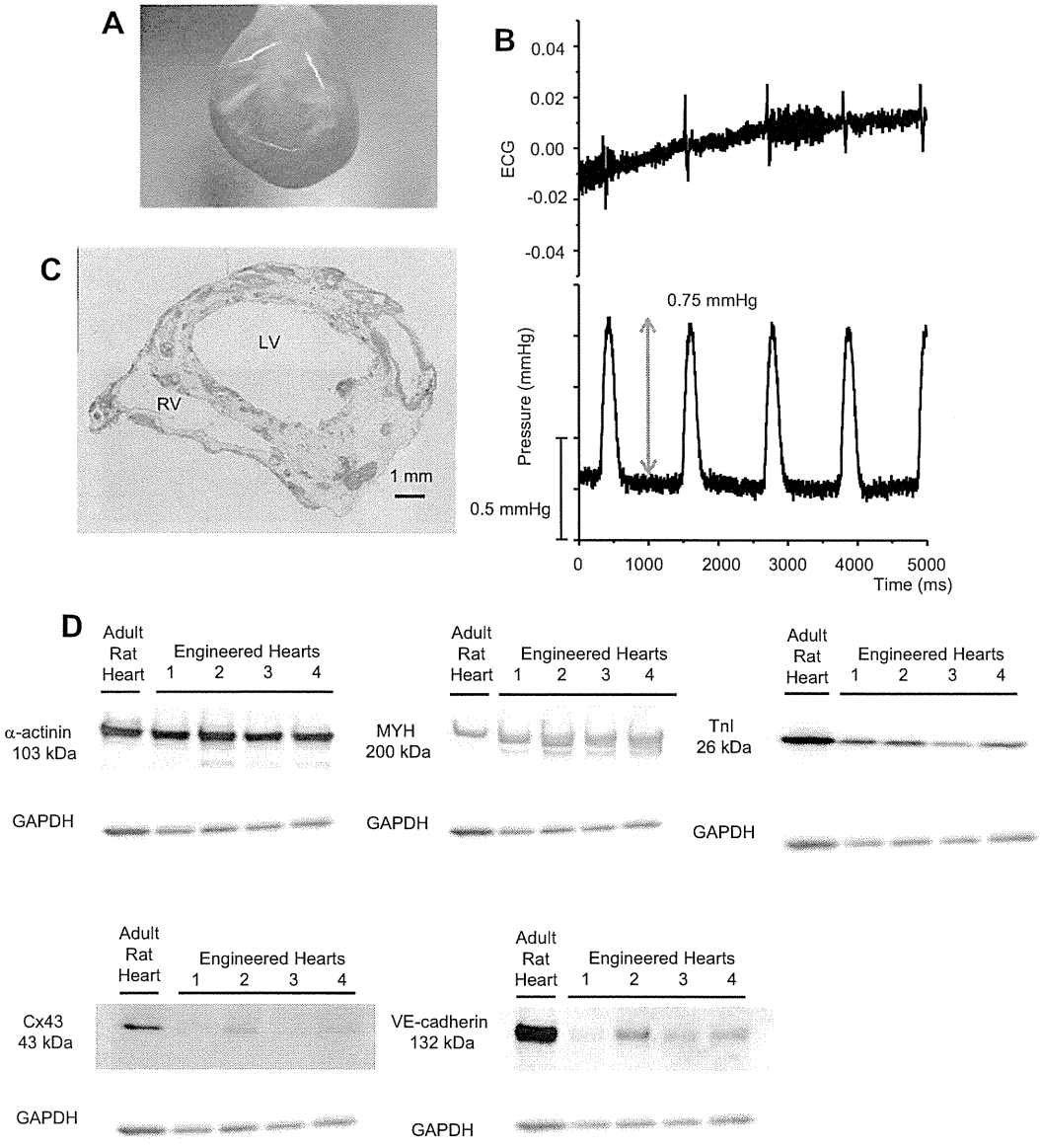

Fig. 4. Properties of recellularized hearts. (A) An image of a recellularized rat heart showing spontaneous beating. (Supplemental movie is available as Movie S2). (B) Real-time tracings of ECG and ventricular pressure are shown. The tracings of ECG and manometry were synchronized and intraventricular pressure was approximately 0.75 mmHg. (C) A microscopic image of a recellularized rat heart in transverse section (H–E staining). Inhomogeneous distribution of seeded cells was observed throughout the heart. Bar indicates 1 mm. (D) Western blot analysis of heart extracts. An adult rat heart and 4 engineered hearts were subjected to western blot analysis. Note the faint expression of VE-cadherin and connexin43 (Cx43) in engineered hearts compared to adult rat heart, in contrast to the abundant expression of sarcomeric alpha actinin, myosin heavy chain (MYH) and cardiac troponin I (TnI), both in engineered and native adult rat hearts.

evaluation revealed an absence of nuclei in the decellularized hearts (Figs. 1C and 2). Immunofluorescent staining demonstrated that collagen I, collagen IV, laminin, and fibronetin remained within the decellularized heart matrix (Fig. 2). Antegrade coronary perfusion with Evans blue dye delineated the extracellular structures of the main coronary arteries (Fig. 1B). The arterial remnants were abruptly terminated. Detailed observation revealed that decellularization procedure destroyed the entire vessel walls in the peripheral arterioles but not in the proximal arteries. This finding may be attributed to sparse extracellular matrices in the peripheral arterioles.

3.2. Whole-heart engraftment of GFP-labeled cells

Live tissue fluorescence imaging of the GFP-labeled seeded cells after antegrade infusion through coronary arteries revealed that the GFP-labeled cardiac cells had extended through the lumens of decellularized coronary arteries into the interstitial spaces at the tip of the remnant coronary arteries (Fig. 3A and Supplementary Movie 1). At day 3, inhomogeneous distribution of the GFP-positive cells was observed throughout the heart tissues. The seeded cells were found in the lumens of coronary arteries as well as in the interstitial matrix (Fig. 3B, C). We also observed that the GFP-positive cells were retained in the heart during the entire observation period (Fig. 3C).

Supplementary video related to this article can be found at http://dx.doi.org/10.1016/j.biomaterials.2014.05.080.

3.3. Recellularization of the decellularized hearts with cardiac cells of neonatal rats

We seeded decellularized rat hearts with freshly isolated neonatal cardiac cells through antegrade coronary perfusion. As the cell isolation procedure did not include techniques such as "pre-plating" method to remove specific cardiac cell types, both cardiomyocytes and other types of cells such as fibroblasts were seeded into the decellularized heart. The 3D organ-like culture was maintained for 8–30 days. Recellularized hearts started spontaneous contraction 2–3 days after recellularization, which continued for 8–30 days (Fig. 4A and Supplementary Movie 2). We

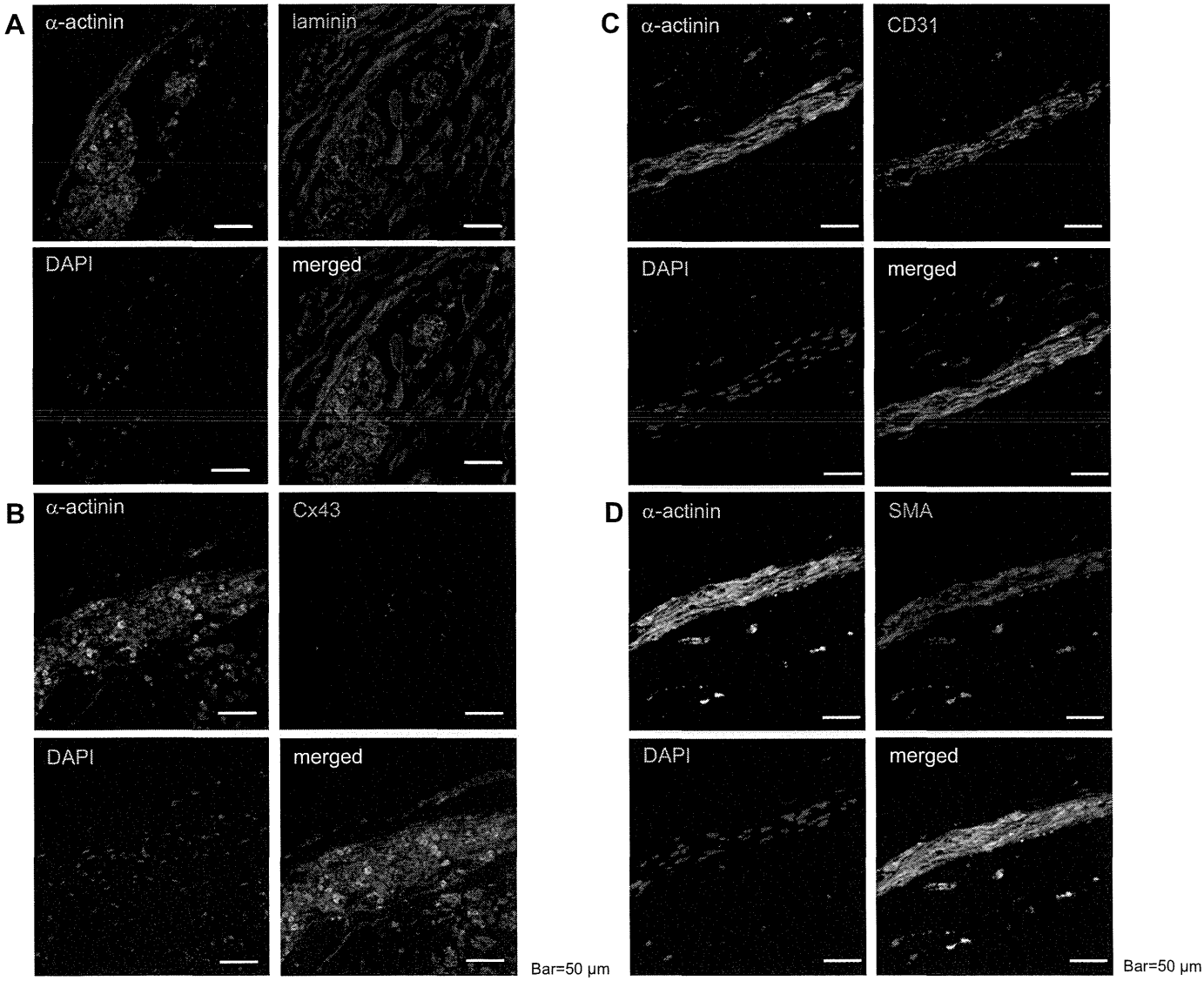

Fig. 5. Immunofluorescence study of recellularized hearts. (A) Sarcomeric alpha actinin-positive cells were surrounded by laminin-positive ECM. (B) Cx43 was sparsely observed among sarcomeric alpha actinin-positive cells. (C), (D) Random alignment of cardiomyocytes, endothelial cells, and smooth muscle cells. The mixture of different cells was observed. Alpha-actinin, CD31, and smooth-muscle-actin were used as cardiac, endothelial, and smooth muscle cell markers, respectively.

recorded electrocardiogram (ECG) and intraventricular pressure. The synchronized tracings of ECG and pressure were shown in Fig. 4B. Microscopic observation revealed that seeded cells adhered inhomogeneously to the decellularized ECM (Fig. 4C). We further examined whether cardiac proteins existed in recellularized hearts by western blot analysis (Fig 4D). As a result, cardiac contractile proteins, including sarcomeric alpha actinin, MYH and cardiac troponin I (TnI), were abundantly observed, while VE-cadherin and Cx43 were only faintly detected in engineered hearts compared to an adult rat heart. Among the seeded cells, sarcomeric alpha actinin positive cells were detected in the ventricles; these cells were surrounded by laminin-positive ECM (Fig. 5A). Although regions of the alpha actinin-positive cells were accompanied by Cx43, the expression was faint, which indicated that intercellular conduction might be immature as compared to adult hearts (Fig. 5B). An immunofluorescence study revealed a randomly-mixed alignment of cardiomyocytes, endothelial cells, and smooth muscle cells stained with alpha actinin, CD31, and smooth muscle (sm)-actin, respectively (Fig. 5C, D). CD31-positive cells and sm-actin-positive cells were not necessarily localized to decellularized vessel-like structures. Transmission Electron Microscope observations showed that the decellularized hearts preserved collagen fibers well in the ECM (Fig. 6A) and the recellularized hearts demonstrated the presence of sarcomeric structures surrounded by ECM (Fig. 6B).

Supplementary video related to this article can be found at http://dx.doi.org/10.1016/j.biomaterials.2014.05.080.

3.4. Excitation-propagation of recellularized hearts

Engineered hearts seeded with GCaMP2-expressing cardiac cells showed spontaneous beating within 2–3 days after recellularization, at which point they were subjected to optical imaging experiments. We observed that spontaneous excitations were generally well aligned and stably propagated in the engineered heart tissues (Fig. 7A and Supplementary Movie 3). Fig. 7A shows the representative images of propagation sequences in an engineered heart. Excitation seemed to emerge in the lateral wall of left ventricle (LV) and propagated through the free LV wall. Isochrone map of the propagating CaT suggested inhomogeneous conduction in substantial areas (Fig. 7C). Conduction velocity (CV) was an order of magnitude or slower (approximately 0.5–5 cm/s) compared to normal adult rat hearts.

Supplementary video related to this article can be found at http://dx.doi.org/10.1016/j.biomaterials.2014.05.080.

3.5. Arrhythmogenicity of recellularized heart tissues

To examine the underlying mechanisms of arrhythmogenesis in the engineered heart tissues and the time-course of maturation in electrical properties, live tissue fluorescence video imaging was employed. We used FFT analysis to examine the synchronicity. Spontaneous excitation of CaT recorded at the three discrete points in the engineered heart tissues were subjected to FFT analysis. In the sample of the first group, during spontaneous beating, the

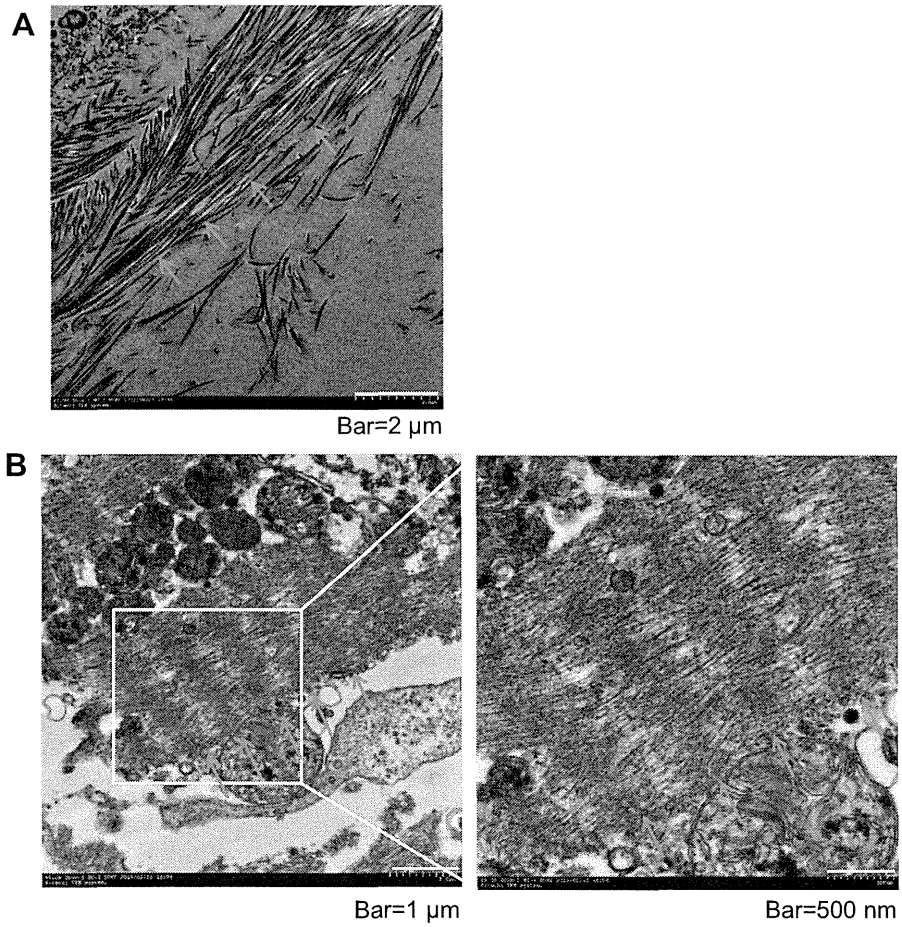

Fig. 6. Ultrastructure of decellularized and recellularized rat hearts by transmission electron microscopy. (A) Ultrastructure of a decellularized heart. Collagen fibers (arrows) in the ECM were well preserved after decellularization procedure. (B) Ultrastructure of a recellularized heart. Arrows show cells with well-organized stria. Cardiac cells seemed to be surrounded by ECM.

entire heart tissues were well-synchronized (Fig. 8A–E and Supplementary Movie 4). Isochrone map showed that excitation propagated rapidly through the left ventricle (Fig. 8D). Frequency analysis showed similar frequency profile pattern at each point (Fig. 8E). On the other hand, in the sample of the second group, although substantial parts of the tissues showed well-organized propagation of excitation, unsynchronized beatings were also observed around ROI-2 (Fig. 9A–E and Supplementary Movie 5). Isochrone map of the propagating CaT showed that initial activation generated from two distinct sites at basal and apical parts of the heart (Fig. 9D). The frequency profiles were accordingly similar at ROI-1 and ROI-3, but not at ROI-2 (Fig. 9E). These observations suggested that there were multiple re-entry like circuits. The sample of the third group exhibited markedly arrhythmogenic characteristics. The heart tissues showed spontaneous contraction, but each region did not show synchronization (Fig. 10A–E and Supplementary Movie 6). Conduction between left and right sides of the heart was hardly observed (Fig. 10D).

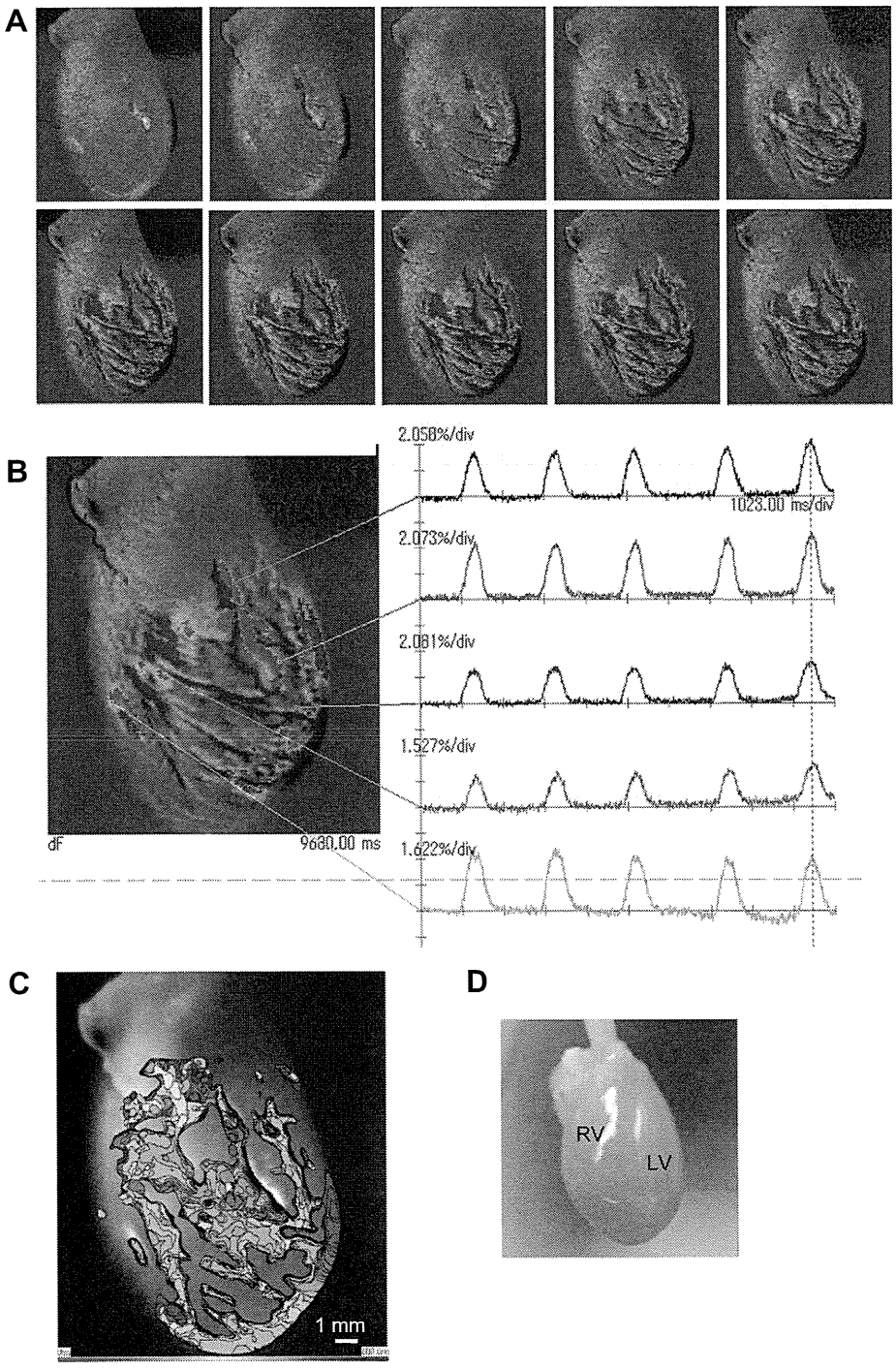

Fig. 7. Propagation of the intracellular calcium transient (CaT) in a recellularized heart. (A) Sequential images in spontaneous beating (every 40 ms). Optical images showed excitation-propagation throughout epicardial surface of the recellularized heart. (B) Detection of the intracellular CaT. (C) Isochrone map (in 10 ms color-coded intervals) of the propagating CaT. Isochrone map suggested inhomogeneous propagation in substantial areas. (D) Anatomical features of the recellularized heart from a frame of video file.

Frequency analysis showed that ROI-1, -2, and -3 beat independently (Fig. 10E). These observations suggested each region had automaticity although cardiac cells were continuously present among ROI-1, -2, and -3.

Supplementary video related to this article can be found at http://dx.doi.org/10.1016/j.biomaterials.2014.05.080.

4. Discussion

In the present study, we successfully constructed 3D engineered hearts by recellularizing adult rat decellularized hearts with neonatal rat cardiac cells, and demonstrated the excitation and propagation properties of 3D engineered heart tissues as an "organ".

For myocardial regeneration therapy of severe heart failure, sufficient wall thickness is required for engrafted cardiac tissues to assist pumping function of the failing hearts. To elucidate the point, several attempts have been made such as "3D cardiac patch" with promoted maturation from ES cell-derived cardiomyocytes [12] or "multi-layered cardiac cell sheets" based on temperature-responsive cell culture dishes [13]. Despite of these efforts, there still remains a limitation in oxygen delivery to thick myocardial tissues, and thus the thickness of the engineered cardiac tissues is confined to approximately 200 μm or less [14,15]. Recent techniques to engineer cardiac tissues with perfusable blood vessels have made thicker vascularized cardiac tissues feasible, which showed spontaneous beating and were transplanted with blood vessel anastomoses [16]. Eschenhagen and Zimmermann

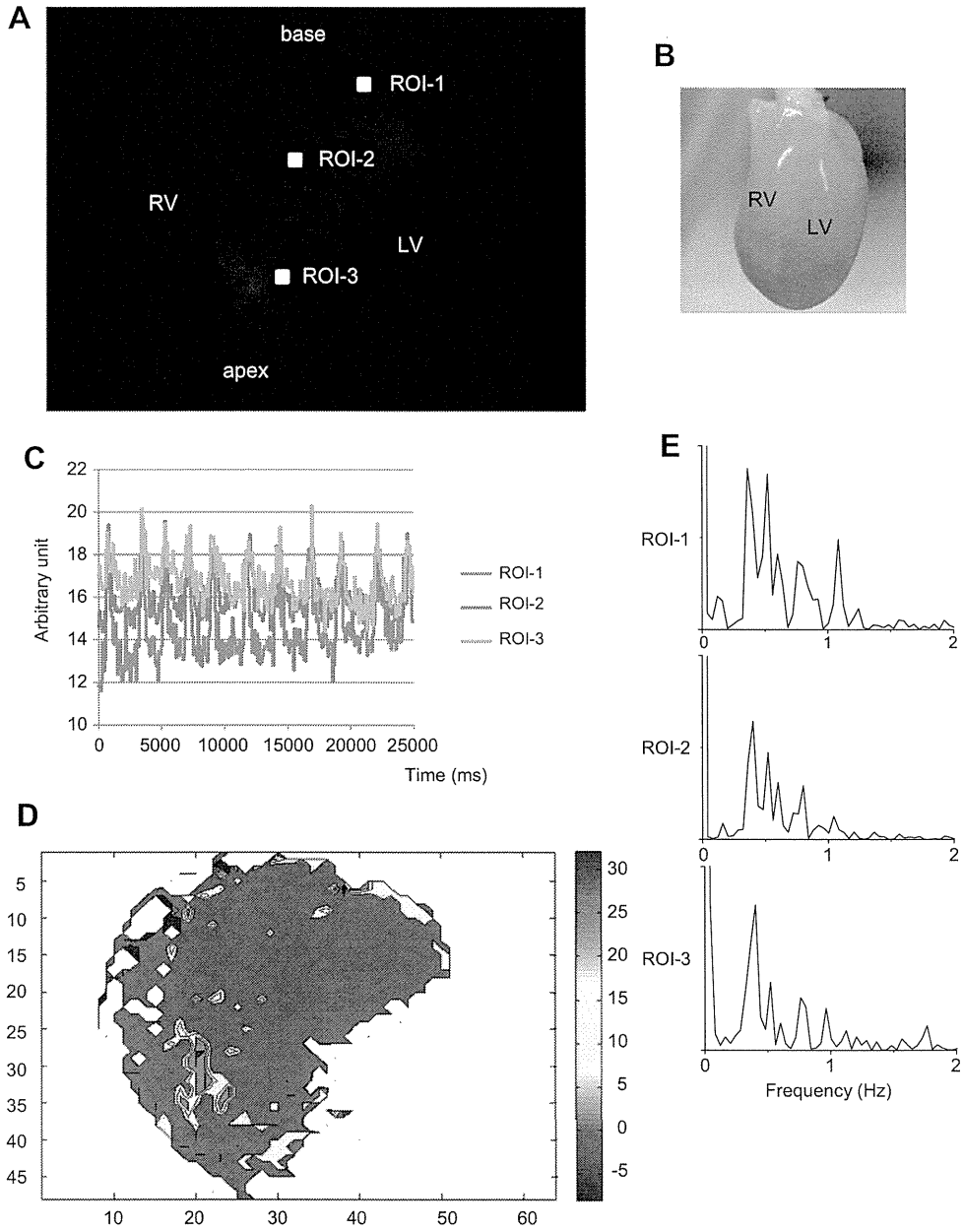

Fig. 8. Propagation of recellularized heart tissues ('well-synchronized' group). (A) Detection of the intracellular CaT driven by local propagation of electrical activity (ROI-1, -2, and -3) in the sample 1. (B) Anatomical features of the recellularized heart from a frame of video file. (C) Intracellular CaT at each site. We observed well-organized conduction of stable excitation in substantial areas of the engineered heart tissues. (D) Isochrone map of the propagating CaT. Note that excitation rapidly propagated throughout the left ventricle. (E) Fast Fourier Transform (FFT) analysis. Note that each site showed similar frequency pattern.

engineered cardiac tissues using a mixture of collagen I, ECM proteins (Matrigel®) and neonatal rat cardiomyocytes into molds; their constructs were intensively interconnected [17]. Their 1–4-mm-thick engineered heart tissue grafts improved the systolic and diastolic functions on implantation in infarcted rat hearts [18].

However, they could not preserve the large-scaled 3D architectures and natural matrix components of the heart. In this context, decellularized whole hearts may act as niches for repopulated cells and vessels for supplying the nutrients to the engineered myocardial constructs. It was indicated that ECM components and preserved mechanical properties of the decellularized heart had directed differentiation of the stem/progenitor cells into the cardiac lineage [19]. This observation also suggests that decellularized heart matrix may therefore be a promising alternative to synthetic scaffolds and a foundation for regenerative efforts for 3D tissue engineering [20].

Previous attempts have revealed that engineered myocardial tissues are not fully synchronized in the small regions of the whole hearts [11,21]. We achieved partial synchronization of significant regions of the heart, but also observed regions which beat independently. Synchronicity is an important factor for the construction of a transplantable artificial organ, since asynchronous regions impair the contractility, as well as potentially increase the risk of lethal cardiac arrhythmias. The calculated CV in our engineered heart tissues was markedly decreased (approximately 5 cm/s) as compared to that reported previously in an adult rat heart [22,23]

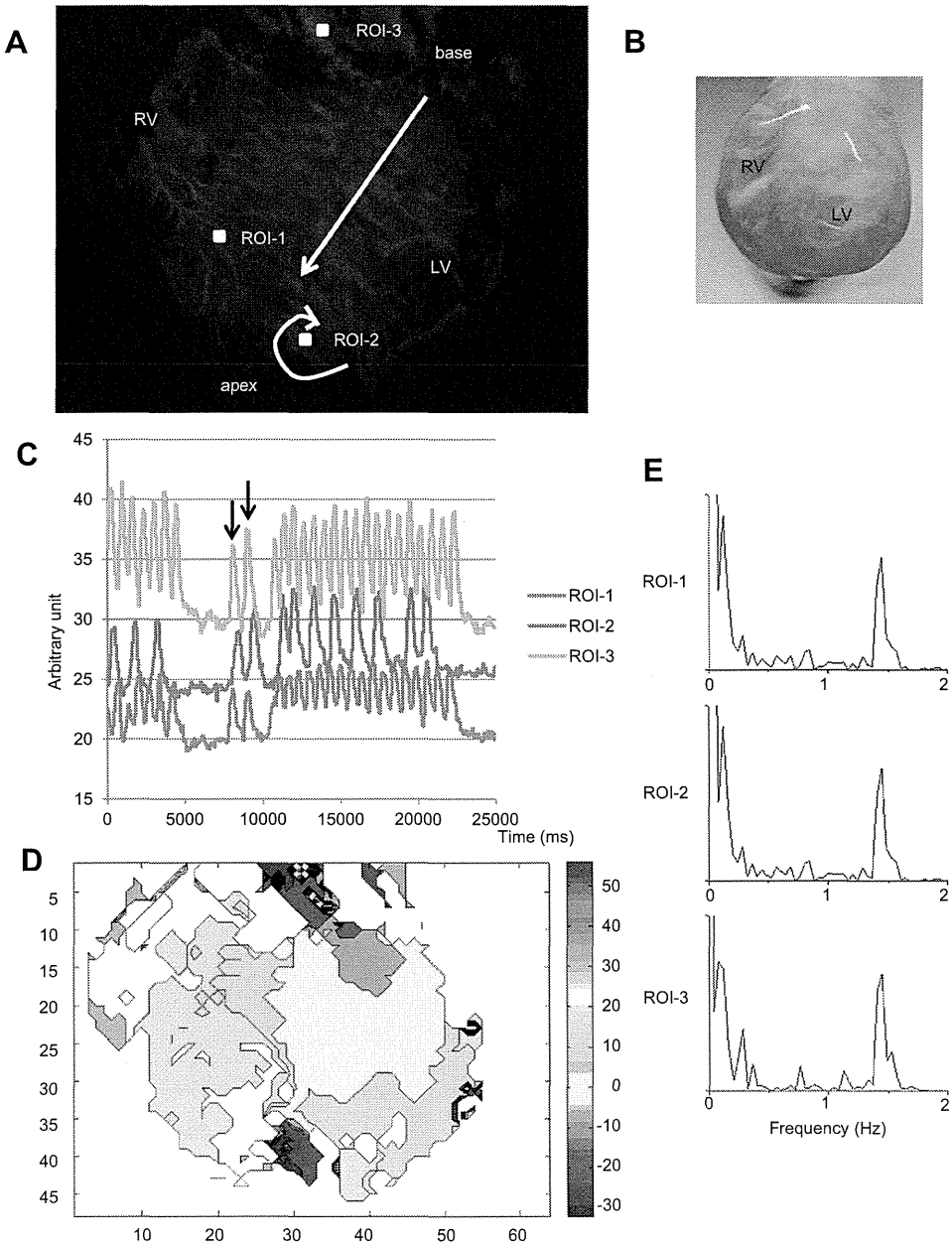

Fig. 9. Propagation of recellularized heart tissues ('unsynchronized' group). (A) Detection of the intracellular CaT driven by local propagation of electrical activity (ROI-1, -2, and -3) in the sample 2. (B) Anatomical features of the recellularized heart from a frame of video file. (C) Intracellular CaT at each site. Propagation of most parts showed the unsynchronized pattern. After 2 beats (arrows), there was a pause, and another wave emerged from the bottom of the heart and collided with the preceding wave. (D) Isochrone map of the propagating CaT. Note that initial activation generated from two distinct sites at basal and apical parts of the heart. (E) FFT analysis. The frequency profiles were similar at ROI-1 and ROI-3, but not at ROI-2. This suggested that at least two excitation-propagation existed.

or in an *in vitro* cultured neonatal rat cardiomyocyte (NRCM), whereas it was similar to that of NRCM with Cx43 mutation [24]. Slow conduction and electrical instability were more apparent in the whole heart. The mixture of automaticity from multiple sites and multiple re-entry leads to arrhythmogenic propensity and obstructs adequate contraction. To create a whole heart with sufficient contraction, electrophysiological evaluation of the whole heart is essential.

Our engineered heart showed a marked decrease in expression of Cx43, which is one of the reasons why our engineered constructs showed slow conduction and electrical instability as well as sparse adhesion of the repopulated cardiomyocytes. This might be improved by overexpressing Cx43 in the engineered cells. Immunofluorescence study revealed randomly mixed alignment of cardiomyocytes, endothelial cells, and smooth muscle cells stained with alpha-actinin, CD31, and sm-actin, respectively; these cells were located close to one another. The mixture of different cells may inhibit smooth electrical conduction. Although these cells were present simultaneously, it is possible that previously resident cadiomyocytes attracted other endothelial cells and attempted to

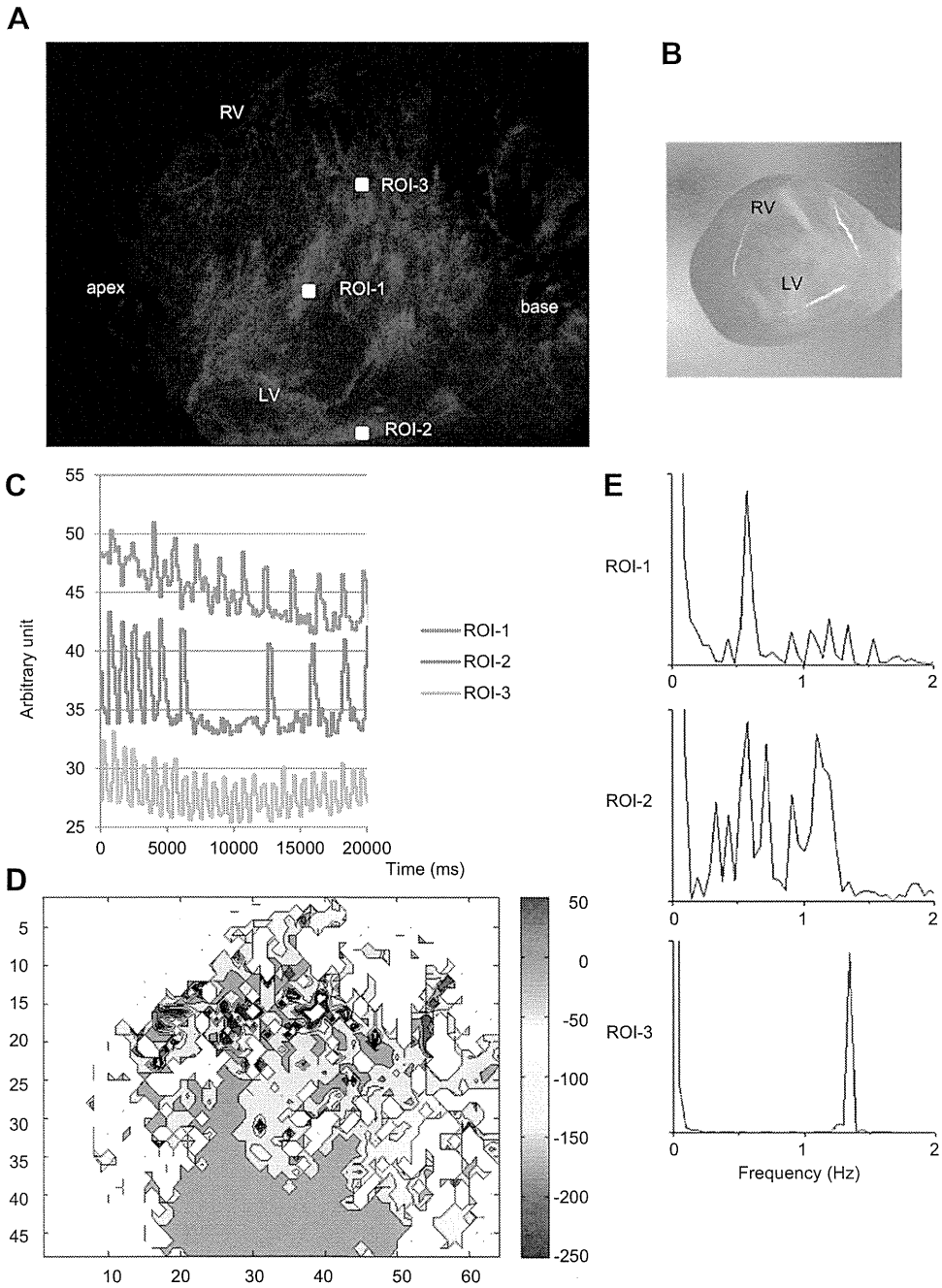

Fig. 10. Propagation of recellularized heart tissues ('disorganized' group). (A) Detection of the intracellular CaT driven by local propagation of electrical activity (ROI-1, -2, and -3) in the sample 3. (B) Anatomical features of the recellularized heart from a frame of video file. The heart sample is shown in the same direction with panels A and D. (C) Intracellular CaT at each site. We recorded disorganized propagation of asynchronous excitation with multiple origins, indicating automaticity. (D) Isochrone map of the propagating CaT. Note that left and right sides of the heart showed distinct automaticity and that conduction between these distinct sites was hardly observed. (E) FFT analysis. Note that each site showed different frequency pattern.

form capillary blood vessels. Cross-talk between endothelial cells and cardiomyocytes regulates not only early cardiac development but also adult cardiomyocyte contraction [25]. Also, it has been reported that the inductive signaling from endothelial cells plays an important role in cardiac conduction system development [26]. The co-existence of endothelial cells and cardiomyocytes may be compatible with this endothelial–cardiomyocyte interaction in the native heart. The density of laminin was high around the resident cardiomyocytes. The finding suggests that cardiomyocytes may produce laminin autonomously in addition to the natural matrix and adapt themselves at the resided space in the matrix. Supplementation with additional extracellular matrices could be possible experiments to attempt.

Extraction of the cadaveric heart *per se* could be potential controversies due to the notion on the death. For example, fabrication of scaffolds analogous to biological tissues using advanced technology such as 3D bioprinting technique may provide clues to solve the issue [27]. The technique has already been applied in various biological tissues including heart valves [28,29] and cartilage [30]. In this regard, 3D bioprinting could be a possible arsenal for heart regeneration in the future, however, arrhythmogenic evaluation as a whole organ will be still essential to create a sufficiently functional heart.

5. Conclusion

We engineered 3D hearts by recellularizing adult rat decellularized hearts with neonatal rat cardiac cells and observed excitation-propagation of spontaneous beatings of the recellularized heart tissues as an "organ". We observed disorganized asynchronous excitation arising from multiple origins while the engineered 3D heart tissues generally showed well-organized stable conduction. Although previous studies have shown the electrophysiological characteristics of 3D engineered heart tissues, those were only limited to the small area of the heart. In the present study, we clearly presented excitation and propagation properties of the entire heart tissues as an "organ". To construct functionally comparable and transplantable artificial heart, our strategy may be beneficial in the evaluation of the arrhythmogenic propensity, and it is necessary to establish the technique to engineer 3D heart tissues with stable excitation-propagation propensity as an organ.

Acknowledgments

We thank Nobu Miyakawa (Osaka University) for technical support of neonatal rat cardiac cell isolation and rat heart decellularization and Ken Shimono, Ph.D. (Panasonic Corporation) for data analysis using MALTAB software.

This work was supported in part by the Japan Society for the Promotion of Science [(Grant-in-Aid for Scientific Research (B), 26293188) (J.L.)].

References

[1] Lozano R, Naghavi M, Foreman K, Lim S, Shibuya K, Aboyans V, et al. Global and regional mortality from 235 causes of death for 20 age groups in 1990 and 2010: a systematic analysis for the Global Burden of Disease Study 2010. Lancet 2012;380:2095–128.
[2] Pfister O, Della Verde G, Liao R, Kuster GM. Regenerative therapy for cardiovascular disease. Transl Res 2014;163:307–20.
[3] Ott HC, Matthiesen TS, Goh S-K, Black LD, Kren SM, Netoff TI, et al. Perfusion-decellularized matrix: using nature's platform to engineer a bioartificial heart. Nat Med 2008;14:213–21.
[4] Ott HC, Clippinger B, Conrad C, Schuetz C, Pomerantseva I, Ikonomou L, et al. Regeneration and orthotopic transplantation of a bioartificial lung. Nat Med 2010;16:927–33.
[5] Petersen TH, Calle EA, Zhao L, Lee EJ, Gui L, Raredon MB, et al. Tissue-engineered lungs for in vivo implantation. Science 2010;329:538–41.
[6] Song JJ, Guyette JP, Gilpin SE, Gonzalez G, Vacanti JP, Ott HC. Regeneration and experimental orthotopic transplantation of a bioengineered kidney. Nat Med 2013;19:646–51.
[7] Nakayama KH, Batchelder CA, Lee CI, Tarantal AF. Decellularized rhesus monkey kidney as a three-dimensional scaffold for renal tissue engineering. Tissue Eng Part A 2010;16:2207–16.
[8] Uygun BE, Soto-Gutierrez A, Yagi H, Izamis M-L, Guzzardi M a, Shulman C, et al. Organ reengineering through development of a transplantable recellularized liver graft using decellularized liver matrix. Nat Med 2010;16:814–20.
[9] Macchiarini P, Jungebluth P, Go T, Asnaghi MA, Rees LE, Cogan TA, et al. Clinical transplantation of a tissue-engineered airway. Lancet 2008;372:2023–30.
[10] Cebotari S, Tudorache I, Ciubotaru A, Boethig D, Sarikouch S, Goerler A, et al. Use of fresh decellularized allografts for pulmonary valve replacement may reduce the reoperation rate in children and young adults: early report. Circulation 2011;124:S115–23.
[11] Lu T-Y, Lin B, Kim J, Sullivan M, Tobita K, Salama G, et al. Repopulation of decellularized mouse heart with human induced pluripotent stem cell-derived cardiovascular progenitor cells. Nat Commun 2013;4:2307.
[12] Zhang D, Shadrin IY, Lam J, Xian H-Q, Snodgrass HR, Bursac N. Tissue-engineered cardiac patch for advanced functional maturation of human ESC-derived cardiomyocytes. Biomaterials 2013;34:5813–20.
[13] Shimizu T, Yamato M, Isoi Y, Akutsu T, Setomaru T, Abe K, et al. Fabrication of pulsatile cardiac tissue grafts using a novel 3-dimensional cell sheet manipulation technique and temperature-responsive cell culture surfaces. Circ Res 2002;90:e40.
[14] Radisic M, Malda J, Epping E, Geng W, Langer R, Vunjak-Novakovic G. Oxygen gradients correlate with cell density and cell viability in engineered cardiac tissue. Biotechnol Bioeng 2006;93:332–43.
[15] Radisic M, Euloth M, Yang L, Langer R, Freed LE, Vunjak-Novakovic G. High-density seeding of myocyte cells for cardiac tissue engineering. Biotechnol Bioeng 2003;82:403–14.
[16] Sekine H, Shimizu T, Sakaguchi K, Dobashi I, Wada M, Yamato M, et al. In vitro fabrication of functional three-dimensional tissues with perfusable blood vessels. Nat Commun 2013;4:1399.
[17] Zimmermann W-H, Schneiderbanger K, Schubert P, Didie M, Munzel F, Heubach JF, et al. Tissue engineering of a differentiated cardiac muscle construct. Circ Res 2002;90:223–30.
[18] Zimmermann W-H, Melnychenko I, Wasmeier G, Didié M, Naito H, Nixdorff U, et al. Engineered heart tissue grafts improve systolic and diastolic function in infarcted rat hearts. Nat Med 2006;12:452–8.
[19] Ng SLJ, Narayanan K, Gao S, Wan ACA. Lineage restricted progenitors for the repopulation of decellularized heart. Biomaterials 2011;32:7571–80.
[20] Song JJ, Ott HC. Organ engineering based on decellularized matrix scaffolds. Trends Mol Med 2011;17:424–32.
[21] Kadota S, Minami I, Morone N, Heuser JE, Agladze K, Nakatsuji N. Development of a reentrant arrhythmia model in human pluripotent stem cell-derived cardiac cell sheets. Eur Heart J 2013;34:1147–56.
[22] Parikh A, Patel D, McTiernan CF, Xiang W, Haney J, Yang L, et al. Relaxin suppresses atrial fibrillation by reversing fibrosis and myocyte hypertrophy and increasing conduction velocity and sodium current in spontaneously hypertensive rat hearts. Circ Res 2013;113:313–21.
[23] Hardziyenka M, Campian ME, Verkerk AO, Surie S, van Ginneken ACG, Hakim S, et al. Electrophysiologic remodeling of the left ventricle in pressure overload-induced right ventricular failure. J Am Coll Cardiol 2012;59:2193–202.
[24] Kizana E, Chang CY, Cingolani E, Ramirez-Correa G a, Sekar RB, Abraham MR, et al. Gene transfer of connexin43 mutants attenuates coupling in cardiomyocytes: novel basis for modulation of cardiac conduction by gene therapy. Circ Res 2007;100:1597–604.
[25] Hsieh PCH, Davis ME, Lisowski LK, Lee RT. Endothelial-cardiomyocyte interactions in cardiac development and repair. Annu Rev Physiol 2006;68:51–66.
[26] Tian Y, Morrisey EE. Importance of myocyte-nonmyocyte interactions in cardiac development and disease. Circ Res 2012;110:1023–34.
[27] Derby B. Printing and prototyping of tissues and scaffolds. Science 2012;338:921–6.
[28] Duan B, Kapetanovic E, Hockaday L a, Butcher JT. Three-dimensional printed trileaflet valve conduits using biological hydrogels and human valve interstitial cells. Acta Biomater 2014;10:1836–46.
[29] Hockaday L a, Kang KH, Colangelo NW, Cheung PYC, Duan B, Malone E, et al. Rapid 3D printing of anatomically accurate and mechanically heterogeneous aortic valve hydrogel scaffolds. Biofabrication 2012;4:035005.
[30] Cui X, Breitenkamp K, Finn MG, Lotz M, D'Lima DD. Direct human cartilage repair using three-dimensional bioprinting technology. Tissue Eng Part A 2012;18:1304–12.
[31] Tallini YN, Ohkura M, Choi BR, Ji G, Imoto K, Doran R, et al. Imaging cellular signals in the heart in vivo: cardiac expression of the high-signal Ca^{2+} indicator GCaMP2. Proc Natl Acad Sci U S A 2006;103(12):4753–8.

ADVANCED HEALTHCARE MATERIALS

Postfach 10 11 61
69451 Weinheim
Germany
Courier services:
Boschstraße 12
69469 Weinheim
Germany
Tel.: (+49) 6201 606 235
Fax: (+49) 6201 606 500
E-mail: advhealthmat@wiley-vch.de

WILEY-VCH

Dear Author,

Please correct your galley proofs carefully and return them no more than three days after the page proofs have been received.

The editors reserve the right to publish your article without your corrections if the proofs do not arrive in time.

Note that the author is liable for damages arising from incorrect statements, including misprints.

Please note any queries that require your attention. These are indicated with red Qs in the pdf or highlighted as yellow queries in the XML working window.

Please limit corrections to errors already in the text; cost incurred for any further changes or additions will be charged to the author, unless such changes have been agreed upon by the editor.

Reprints may be ordered by filling out the accompanying form.

Return the reprint order form by fax or by e-mail with the corrected proofs, to Wiley-VCH: **advhealthmat@wiley-vch.de**

To avoid commonly occurring errors, please ensure that the following important items are correct in your proofs (please note that once your article is published online, no further corrections can be made):

- **Names** of all authors present and spelled correctly
- **Titles** of authors correct (Prof. or Dr. only: please note, Prof. Dr. is not used in the journals)
- **Addresses** and **postcodes** correct
- **E-mail address** of corresponding author correct (current email address)
- **Funding bodies** included and grant numbers accurate
- **Title** of article OK
- All **figures** included
- **Equations** correct (symbols and sub/superscripts)
- Note: the **resolution of the figures** in the system and the PDF proofs is intentionally of lower quality to avoid slow loading times. Your high-resolution files will be used for the final publication.

Please note: If you send any additional information, such as figures or other display items, to advhealthmat@wiley-vch.de, please also indicate this clearly in the XML working window by inserting a comment using the query tool.

ADVANCED HEALTHCARE MATERIALS

Reprint Order Form 2015
- please return with your proofs -

Editorial Office:

Wiley-VCH Verlag, Boschstrasse 12
69469 Weinheim, Germany

Tel.: (+49) 6201 606 235
Fax: (+49) 6201 606 500

E-mail: advhealthmat@wiley-vch.de
http://www.advhealthmat.de

Manuscript No. _____

Please send me and bill me for

☐ no. of **reprints** via ☐ airmail (+ 25 Euro) ☐ surface mail

☐ **high-resolution PDF file** (330 Euro).

My e-mail address:

_____

Please note: It is not permitted to present the PDF file on the internet or on company homepages

★**Special Offer**★ If you order 200 or more reprints you will get a PDF file for half price.

Information regarding VAT
Please note that from German sales tax point of view, the charge for **Reprints, Issues or Posters** is considered as **"supply of goods"** and therefore, in general, such delivery is a subject to German sales tax. However,this regulation has no impact on customers located outside of the European Union. Deliveries to customers outside the Community are automatically tax-exempt. Deliveries within the Community to institutional customers outside of Germany are exempted from the German tax (VAT) only if the customer provides the supplier with his/her VAT number. The VAT number (value added tax identification number) is a tax registration number used in the countries of the European Union to identify corporate entities doing business there. It starts with a country code (e.g. FR for France, GB for Great Britain) and follows by numbers.

Cover Posters

Posters are available of all the published covers and frontispieces in two sizes

☐ DIN A2 42 x 60 cm/ 17 x 24in (one copy: **39 Euro**)

☐ DIN A1 60 x 84 cm/ 24 x 33in (one copy: **49 Euro**)

Postage for shipping posters overseas by airmail:
+ 25 Euro

Postage for shipping posters within Europe by surface mail:
+ 15 Euro

Mail reprints / cover posters to:

_____
_____
_____
_____
_____

Invoice address:

_____
_____
_____
_____
_____

_____
Date, Signature **Stamp**

VAT no.: _____
(institutes / companies in EU countries only)

Purchase Order No.: _____

Credit Card Payment

VISA, MasterCard, AMERICAN EXPRESS
Please use the Credit Card Token Generator located at the website below to create a token for secure payment. The token will be used instead of your credit card number.

Credit Card Token Generator:
https://www.wiley-vch.de/editorial_production/index.php

Please transfer your token number to the space below.

Credit Card Token Number:

Price list for reprints (The prices include mailing and handling charges. All Wiley-VCH prices are exclusive of VAT)

No. of pages	Price (in Euro) for orders of					
	50 copies	100 copies	150 copies	200 copies	300 copies	500 copies
1-4	345	395	425	445	548	752
5-8	490	573	608	636	784	1077
9-12	640	739	786	824	1016	1396
13-16	780	900	958	1004	1237	1701
17-20	930	1070	1138	1196	1489	2022
for every additional 4 pages	147	169	175	188	231	315

★ **Special Offer** ★ If you order 200 or more reprints you will get a PDF file for half price.

Wiley-VCH Verlag GmbH & Co. KGaA; Location of the Company: Weinheim;
Chairman of the Supervisory Board: Stephen Michael Smith,
Trade Register: Mannheim, HRB 432833, General Partner: John Wiley & Sons GmbH,
Location: Weinheim, Trade Register Mannheim, HRB 432296,
Managing Directors: Dr. Jon Walmsley

WILEY-VCH

xxxx

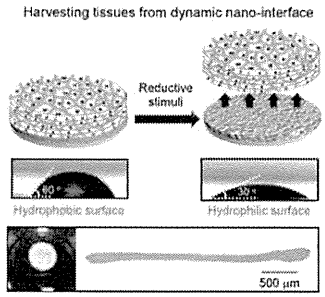

Functional 3D-engineered tissues are successfully harvested from a substrate using stimuli-responsive hydrogel films with dynamic nano-interface. The dynamic wettability control at the interfaces allows for cellular detachment, leading to tissue harvesting without serious damage and remaining polymers. This method can be applied to various types of organs and used for tissue transplantation in regenerative medicine.

ADHM201500065(201500065)

Materials Views
www.MaterialsViews.com

ADVANCED HEALTHCARE MATERIALS
www.advhealthmat.de

Dynamic Nano-Interfaces Enable Harvesting of Functional 3D-Engineered Tissues

*Akihiro Nishiguchi, Michiya Matsusaki, Shigeru Miyagawa, Yoshiki Sawa, and Mitsuru Akashi**

Keywords: cell adhesion, dynamic interface, gels, thin films, tissue engineering

A significant development in stem cell research with embryonic stem cells (ES cells) and induced pluripotent stem cells (iPS cells) has promoted not only clinically relevant therapies in regenerative medicine but also the establishment of disease-specific models for drug discovery.[1] The use of stem cells as a cell source has the enormous potential for a cell transplantation alternative to organ transplants, which is plagued by chronic donor organ shortages.[2] However, the injection of suspended cells into diseased tissues has failed because of the loss of cells and extremelylow graft survival rates.[3] To overcome this problem, a tissue transplantation approach based on tissue engineering concepts has attracted increasing attention in the biomedical fields.[4] A number of functional polymeric materials have been reported in the in vitro fabrication of tissues with highly organized 3D structures of cells and extracellular matrices (ECMs),[5] but these may give rise to serious adverse effects such as immunogenicity and inflammatory responses to the surrounding materials. A scaffold-free tissue transplantation that employs only cells and tissues would be useful as an innovative therapeutic method.[6]

To this end, cultured cells and tissues need to be harvested from substrates. However, the enzymatic treatment for detachment of cells such as trypsin breaks not only cell-substrate adhesion but also cell–cell connections, leading to failures in tissue harvesting. Therefore, substrates with stimuli-responsive interfaces that selectively switch cell-substrate adhesion to weaken should be designed for the detachment with the cell–cell connections. Several researchers have reported the design of stimuli-responsive substrates such as photoresponsive substrates,[7a,b] host–guest interactions,[7c] and protein interactions[7d] for the control of cell adhesion. One of the most successful methods is cell sheet engineering that can be used to detach cultured cell-monolayers from temperature-responsive dishes grafted with poly(*N*-isopropylacrylamide) (PIPAAm) on the surface.[8] When above the lower critical solution temperature (LCST) near 32 °C, cells adhere to hydrophobic surfaces, while decreasing temperatures below the LCST changes to the hydrophilic surfaces by hydration of grafted PIPAAm. This transition in surface hydrophobicity causes cells to detach through the dissociation of proteins. However, since it is difficult for water molecules to approach polymer chains grafted on solid substrates and dehydrated polymers and aggregations remain,[9] the responsiveness during the swelling process is low. Moreover, existing methods also have drawbacks including the use of temperature decrease and photoreaction that do not occur in living body, limitations in applicable substrates, some damage during the process of harvesting and stacking, and difficulties in harvesting functional tissues.

We previously reported a hydrogel scaffold comprising disulfide-cross-linked poly(γ-glutamic acid) (γ-PGA-SS) to construct large and thick 3D tissues by seeding cells and degrading hydrogels.[10] γ-PGA-SS hydrogels have reductant-responsive properties originating in the cleavage of disulfide cross-linking points to thiol groups with reductants, which leads to the degradation of γ-PGA polymer matrices to form tissues composed of cells and ECMs secreted from cells. We consider that surfaces of stimuli-responsive hydrogels exhibit hydrophobic to hydrophilic changes because γ-PGA hydrogels have hydrophobic property due to the methylene units in both main chains and cross-linker (Figure S1, Supporting Information). When the polymer networks cross-linked with disulfide bonds are cleaved in response to reducing agents, highly mobile dangling chains with hydrophilic carboxylic and thiol groups will be exposed.[11] In this system, rapid responsiveness occurs because water molecules exist in large quantities around hydrogels and can easily approach polymer chains. Dynamic control of the wettability on nano-interfaces can be used to harvest cells and functional tissues without damaging the tissues.

Here we report a novel method to harvest functional 3D-engineered tissues using stimuli-responsive gel films where the surface wettability can be dynamically controlled (**Figure 1**). The 3D tissues were constructed by a cell-accumulation technique, which is based on fibronectin (FN) and gelatin (G) nanofilms (FN-G nanofilms) coated onto cell surfaces,[12] on micrometer-sized thin films of γ-PGA-SS hydrogels. We addressed dynamic property changes of wettability and structures on nano-interfaces in response to reductants. We attempted hydrophobic to hydrophilic changes on nano-interfaces allowed for harvesting functional 3D-tissues such as vascularized fi-

A. Nishiguchi, Dr. M. Matsusaki, Prof. M. Akashi, Department of Applied Chemistry, Graduate School of Engineering, Osaka University, 2–1 Yamada-oka Suita, Osaka 565–0871, Japan (E-mail: akashi@chem.eng.osaka-u.ac.jp)
Dr. S. Miyagawa, Prof. Y. Sawa, Department of, Surgery, Division of Cardiovascular Surgery, Graduate School of Medicine, Osaka University, 2–2 Yamada-oka Suita, Osaka 565–0087, Japan
Correspondence to: Prof. M. Akashi (E-mail: akashi@chem.eng.osaka-u.ac.jp)
10.1002/adhm.201500065

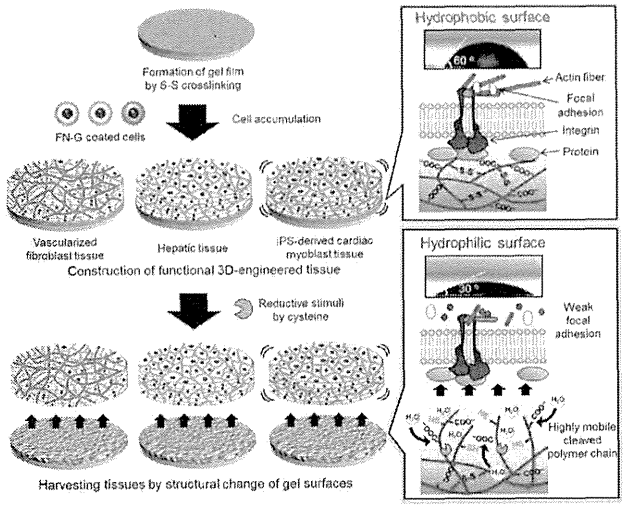

Figure 1. Schematic illustration of the harvesting process of 3D-engineered tissues from reductant-responsive gel films of disulfide-cross-linked γ-PGA (γ-PGA-SS). Pre-gel solutions containing γ-PGA, EDC, and cystamine (cross-linker) were thinly coated on substrates by almost-complete aspiration of the solution. The cross-linking reaction of amine groups with carboxylic groups proceeded within 10 min to form gel films on the substrate. 3D tissues constructed by a cell-accumulation technique onto gel films were exposed to cysteine-containing media, leading to harvesting various tissues including vascularized fibroblast tissues, liver tissues, and heart tissues from substrates. During this process, hydrophobic to hydrophilic changes at interfaces between gel films and tissues occurred dynamically through exchange reactions between thiol groups in cysteine and disulfide cross-linking bonds.

broblast tissues, hepatic tissues, and iPS-derived cardiac myoblast tissues without giving rise to serious physical damage.

The harvesting technique of 3D tissues consists of two-step processes during hydrogel formation and the degradation of gels by cleaving thiol groups. Pre-gel solutions containing γ-PGA, 1-ethyl-3-(3-dimethylaminopropyl) carbodiimide (EDC), and cystamine were added to substrates. Since thick hydrogel films (>1 mm) showed low cell-adhesive properties (data not shown), thin hydrogel films were employed due to their higher cell-adhesive property partly because mechanical properties like stiffness were affected by the distance from substrates.[13] We selected *trans*-well insert membranes with 8 μm pores as a substrate to promote the diffusion of nutrients and reductants from basal porous membranes. Cross-linking reactions via the formation of amide bonds were confirmed by FT-IR and ^{1}H NMR analyses (Figure S2, Supporting Information). Cross-linking densities, gelation times, and swelling ratios varied with the concentration of γ-PGA and molar ratio of EDC and cystamine (Table 1, Supporting Information). In the following experiments, hydrogels of 6–1–1 (wt% of γ-PGA, [EDC]/[γ-PGA], and [NH_2]/[COOH] were used due to the suitable stability and swelling ratio.

The formation of 6–1–1 gel films of γ-PGA-SS was optimized by quartz crystal microbalance (QCM) analyses, which estimated the film thickness as approximately 70 nm from frequency shifts in a dry form (Figure S3, Supporting Information). These γ-PGA-SS gel films possessed highly swellable properties (swelling ratio: 10) due to carboxylate anion in main chains and color 3D laser scanning microscopy observations showed that the thickness in wet conditions was approximately 5 μm at centers of membrane (**Figure 2**a). The resulting gel films displayed smooth surface structures and filled almost all pores. To evaluate the stimuli responsiveness of γ-PGA-SS gel films, we started with QCM analyses that measure weight loss in a bulk state (Figure 2b). The weight loss depending on the concentration of cysteine was confirmed, although there was little change of the weight for 1 h of incubation. The production of thiol groups by cleaving disulfide bonds in response to reductants was confirmed by FT-IR spectra and UV–vis measurement using Elman assay (Figure S4, Supporting Information). To investigate how reducing-stimuli alter surface structures and wettability, atomic force microscope (AFM) observations and contact angle measurements of gel films in a swollen state were performed (Figure 2c,d). Originally smooth gel films increased in roughness after 1 h of incubation to form markedly uneven surfaces after 24 h (Figure 2c). Interestingly, contact angles drastically decreased within 1 min in response to incubation with cysteine and altered from 58° to 32° in just 1 h (Figure 2d). Therefore, the hydrophilicity of gel surfaces dynamically increased through reduction reactions, indicating surface property of gel films drastically changed even though the weight in a bulk state did not change for 1 h. Moreover, we performed QCM-D analyses for real-time measurements of the thickness and shear elasticity in a flow state, especially in the early process of degradation (Figure 2e). These values were calculated from viscoelastic analyses of frequency shifts (Δf) and energy dissipation change (ΔD) using Voigt-based model (Figure S5, Supporting Information). As a result, the film thickness slightly decreased after incubation with cysteine and shear elasticity increased in the early process, indicating high responsiveness at interfaces. These results from gel films were in agreement with that of mechanical properties of gels in bulk state, which showed increases in rupture strength and shear elastic modulus after degradation (Figure S6, Supporting Information). These results suggest that cleaving disulfide bonds exposed highly mobile dangling chains with hydrophilic carboxylic and thiol groups to interfaces, resulting in increases in wettability and shear stress. Adhesiveness of cells and proteins to materials strongly depends on surface properties such as size, conformation, stiffness, wettability, and interactions.[14] Therefore, unique nano-interfaces with dynamic structure-changes including roughness, hydrophilicity, and the structure of polymer chains can be used to control cellular adhesion and detachment.

To evaluate whether cells dynamically respond to wettability changes in nano-interfaces by reducing agents, the morphology of normal human dermal fibroblasts (NHDFs) incubated on γ-PGA-SS 6–1–1 gel films was observed at the single-cell level. NHDFs adhered and extended well in 1 day on gel films, which were coated with fibronectin. Soon after the addition of